

DRAFT VERSION

Detectability of [C II] 158 μm emission from high-redshift galaxies: predictions for ALMA and SPICA

Kentaro Nagamine¹, Arthur M. Wolfe¹, Lars Hernquist²

ABSTRACT

We discuss the detectability of high-redshift galaxies via [C II] 158 μm line emission by coupling an analytic model with cosmological Smoothed Particle Hydrodynamics (SPH) simulations that are based on the concordance Λ cold dark matter (CDM) model. Our analytic model describes a multiphase interstellar medium (ISM) irradiated by the far ultra-violet (FUV) radiation from local star-forming regions, and it calculates thermal and ionization equilibrium between cooling and heating. The model allows us to predict the mass fraction of a cold neutral medium (CNM) embedded in a warm neutral medium (WNM). Our cosmological SPH simulations include a treatment of radiative cooling/heating, star formation, and feedback effects from supernovae and galactic winds. Using our method, we make predictions for the [C II] luminosity from high-redshift galaxies which can be directly compared with upcoming observations by the *Atacama Large Millimeter Array* (ALMA) and the *Space Infrared Telescope for Cosmology and Astrophysics* (SPICA). We find that the number density of high-redshift galaxies detectable by ALMA and SPICA via [C II] emission depends significantly on the amount of neutral gas which is highly uncertain. Our calculations suggest that, in a CDM universe, most [C II] sources at $z = 3$ are faint objects with $S_\nu < 0.01$ mJy. Lyman-break galaxies (LBGs) brighter than $R_{AB} = 23.5$ mag are expected to have flux densities $S_\nu = 1 - 3$ mJy depending on the strength of galactic wind feedback. The recommended observing strategy for ALMA and SPICA is to aim at very bright LBGs or star-forming DRG/BzK galaxies.

Subject headings: cosmology: theory — stars: formation — galaxies: formation — galaxies: evolution — methods: numerical

¹ Center for Astrophysics and Space Sciences, University of California, San Diego, MC 0424
9500 Gilman Dr., La Jolla, 92093-0424 Email: knagamine@ucsd.edu, awolfe@ucsd.edu

²Harvard University, 60 Garden Street, Cambridge, MA 02138

1. Introduction

Up to now, the high-redshift galaxies detected in large numbers are observed by the radiation from stars in rest-frame UV to optical wavelengths. Such studies have been fruitful in delineating the properties of star-forming galaxies at $z \gtrsim 3$ that are bright in UV; i.e., the Lyman-break galaxies (LBGs) (e.g., Steidel et al. 1999; Adelberger & Steidel 2000; Shapley et al. 2001; Iwata et al. 2003; Steidel et al. 2003; Ouchi et al. 2004a,b). Within the hierarchical galaxy formation paradigm based on the cold dark matter (CDM) model (Blumenthal et al. 1984; Davis et al. 1985), it has been shown that the spectro-photometric properties of LBGs can be accounted for if we associate them with relatively massive galaxies ($M_\star \gtrsim 10^{10} M_\odot$) situated in large dark matter halos ($M_{\text{halo}} \gtrsim 10^{12} M_\odot$) (e.g. Mo & Fukugita 1996; Davé et al. 1999; Nagamine 2002; Weinberg et al. 2002; Nagamine et al. 2004d, 2005b,a; Night et al. 2006; Finlator et al. 2006).

However, observing the UV light emitted by the young stars does not directly tell us about how much gas there is in the galaxy. In order to obtain a full picture of galaxy formation, we need to find answers to the questions such as: 1) How much neutral gas is available for star formation in high-redshift galaxies? 2) What is the baryonic mass (in particular, the neutral hydrogen mass) fraction as a function of halo mass, and how does it evolve as a function of redshift? 3) How does the volume-averaged neutral gas mass density evolve as a function of redshift? 4) What are the main cooling and heating processes of the ISM in high-redshift galaxies?

One of the ways to detect the neutral hydrogen in high-redshift galaxies is to search for damped Lyman- α absorbers (DLAs, Wolfe et al. 2005, for a review) in quasar absorption lines. DLAs are defined as quasar absorption systems with a neutral hydrogen column density $N_{\text{HI}} > 2 \times 10^{20} \text{cm}^{-2}$, a threshold column density that effectively guarantees gas neutrality at high redshifts (Wolfe et al. 1986, 2005). Since DLAs are known to dominate the neutral hydrogen mass density at $z \gtrsim 3$ (e.g., Lanzetta et al. 1995; Storrie-Lombardi & Wolfe 2000), it is expected that they represent a significant reservoir of neutral gas for star formation. A large number of DLAs have been discovered at $z \gtrsim 3$, and they have proven to be one of the best probes of neutral gas in high-redshift galaxies, complementary to the optical to infra-red (IR) observations. A recent search for DLAs in the Sloan Digital Sky Survey (SDSS) data archive yielded a large sample of over 500 DLAs at $z > 2.2$ (Prochaska & Herbert-Fort 2004; Prochaska, Herbert-Fort, & Wolfe 2005). These observational results are beginning to put stringent constraints on theoretical/numerical models of galaxy formation. Furthermore, Wolfe et al. (2003b) opened a new window for probing star formation in high-redshift DLA galaxies utilizing the CII* absorption lines, and this paper is motivated by their work.

The CII* absorption lines originate from the excited $^2P_{3/2}$ state in the ground $2s^2 2p$ term

of C^+ . This is the same state that gives rise to $[C\text{ II}]$ emission at $\lambda = 157.74\ \mu\text{m}$ through the $^2P_{3/2} \rightarrow ^2P_{1/2}$ fine structure transition. Because this is the dominant coolant of diffuse ISM at temperatures $T \leq 5000\text{ K}$ (Dalgarno & McCray 1972; Tielens & Hollenbach 1985; Wolfire et al. 1995; Lehner et al. 2004), detection of $[C\text{ II}]$ emission is potentially another method for finding cold neutral gas at high redshifts (Petrosian et al. 1969; Loeb 1993).

$[C\text{ II}]$ emission was first detected towards the inner regions of gas-rich spiral galaxies and starburst galaxies; i.e., dense star-forming gas irradiated by UV radiation from young star-forming regions near galactic centers (Russell et al. 1980; Crawford et al. 1985; Stacey et al. 1991; Carral et al. 1994). In this case, the brightness of the emission line suggests that it is produced in warm ($T > 200\text{ K}$), dense ($n_{\text{H}} > 10^3\text{ cm}^{-3}$) photodissociated regions (PDRs) with pressures $P/k_B = 10^4 - 10^7\text{ K cm}^{-3}$ at the interface between giant molecular clouds and fully ionized media. The $[C\text{ II}]$ luminosity accounts for $0.1 - 1\%$ of the total far-IR luminosity of the nuclear regions.

However, later space-based observations with the Long Wavelength Spectrometer (LWS) on-board ESA’s Infrared Space Observatory (ISO) have shown that, for quiescent late-type galaxies like NGC6946, the $[C\text{ II}]$ emission from extended diffuse gas over the entire disk could also be significant compared to that from dense compact star-forming gas (e.g., Madden et al. 1993; Malhotra et al. 1997; Leech et al. 1999; Malhotra et al. 2001; Contursi et al. 2002). The diffuse cold components of the ISM seems to be at least as important sources of the $[C\text{ II}]$ emission as are compact regions (e.g., Sauty et al. 1998; Pierini et al. 1999; Pierini et al. 2001; Contursi et al. 2002).

More recently, $[C\text{ II}]$ emission has also been detected in the highest redshift SDSS quasar at $z = 6.42$ (Maiolino et al. 2005). Quasars are considered to host significant amounts of molecular gas ($M_{\text{gas}} \approx 10^{11} M_{\odot}$) and dust ($M_{\text{dust}} \approx 10^8 M_{\odot}$), and are therefore forming stars at a significant rate of $SFR \gtrsim 1000 M_{\odot} \text{ yr}^{-1}$ (e.g., Omont et al. 1996, 2001, 2003; Carilli et al. 2001; Walter et al. 2003; Beelen et al. 2004; Carilli et al. 2004). Given this large amount of gas contained in them, they should be very bright in $[C\text{ II}]$ luminosity, allowing them to be easily detected even at very high redshift. However, bright quasars have much lower comoving space density than LBGs and are not representative of the entire galaxy population; they are special sources hosting supermassive black holes, and may be in unusual dynamical states if their activity is triggered by mergers (e.g., Hopkins et al. 2005).

The detection of $[C\text{ II}]$ emission from normal (i.e., not quasars or active galactic nuclei [AGN]) high-redshift star-forming galaxies would be a more *direct* way than the absorption line technique to find out about the amount of neutral gas available for star formation. Such detections of $[C\text{ II}]$ emission from high-redshift galaxies, for example, by ALMA and SPICA, would set an important constraint on the theory of galaxy formation. In particular

interferometric maps of [C II] emission would reveal the spatial dimensions of the DLAs, a property that so far has eluded detection. By combining these measurements with the velocity widths of the [C II] emission lines, it will be possible to infer the dark matter masses of these objects, and the luminosity of the [C II] emission lines would tell us the heating rate of the gas.

In this paper we study the detectability of high-redshift DLA galaxies by coupling an analytic model with cosmological SPH simulations that are based on the concordance Λ CDM model, and make predictions for upcoming observations by ALMA and SPICA. We also compare the computed [C II] luminosity function with the observed LBG luminosity function, and discuss the connection between DLA galaxies and LBGs. Stark (1997) discussed the potential measurement of [C II] emission from high-redshift galaxies, but he made various assumptions for the [C II] luminosity function and the evolution of the characteristic luminosity based on the local observations and numerical simulations, and focused more on the observing time and conditions rather than the intrinsic nature of high-redshift galaxies. The present study extends his original work, and is intended to be more physically motivated by using full cosmological hydrodynamic simulations which simulate structure formation from early epochs to the present time. We note that Sugimoto et al. (1999) studied the detectability of atomic emission lines of carbon, nitrogen, and oxygen, but they focused on the intensity fluctuations owing to sources at $z \sim 10$ rather than the detection of individual objects.

2. Cosmological Hydrodynamic Simulations

The cosmological Smoothed Particle Hydrodynamics (SPH) simulations that we use in this paper were carried out using GADGET-2 (Springel 2005). This code adopts the novel ‘entropy-formulation’ of SPH (Springel & Hernquist 2002), and includes ‘standard’ physical processes such as radiative cooling and heating by a uniform UV background of modified Haardt & Madau (1996) form (see Davé et al. 1999), star formation, supernova feedback, as well as a phenomenological model for feedback by galactic winds. The latter allows us to examine the effect of galactic outflows. (For now, we do not account for feedback associated with black hole growth, as in, e.g., Springel et al. (2005b,a); Di Matteo et al. (2005), but plan to investigate consequences of this mechanism in due course.) The ionization equilibria of hydrogen and helium are solved assuming an optically thin limit throughout the simulation box. We will discuss this point in Section 4.2. We utilize a series of simulations of varying box-size and particle number to isolate the impact of numerical resolution on our results. The important parameters of the simulation runs are summarized in Ta-

ble 1. The same simulations were used for the study of the cosmic star formation history (Springel & Hernquist 2003b; Nagamine et al. 2004a), LBGs at $z = 3 - 6$ (Nagamine et al. 2004d; Night et al. 2006; Finlator et al. 2006), damped Lyman- α systems (Nagamine et al. 2004b,c, 2005c), massive galaxies at $z = 2$ (Nagamine et al. 2005b,a), and the intergalactic medium (Furlanetto et al. 2003, 2004, 2005). The adopted cosmological parameters of all runs are $(\Omega_M, \Omega_\Lambda, \Omega_b, \sigma_8, h) = (0.3, 0.7, 0.04, 0.9, 0.7)$, where $h \equiv H_0/(100 \text{ km s}^{-1} \text{ Mpc}^{-1})$ is the Hubble constant. We also use the notation $h_{70} \equiv h/0.7$.

The initial conditions for our simulations are set by tiny density fluctuations as motivated by inflationary theories, and the calculations follow the development of structure using the laws of gravity and hydrodynamics. Therefore, in principle the cosmological simulations allow us to model galaxy evolution in a physical manner. However, even with current state-of-the-art computers, we still lack the computational resources to directly simulate the details of the ISM dynamics below $\sim 1 \text{ kpc}$ while at the same time solving for large-scale structure formation on tens of megaparsecs. Consequently, the simulations that we utilize in this paper do not directly resolve the multiphase nature of the ISM with temperature $T < 10^4 \text{ K}$, but keep track of the dynamics of the hot ionized medium (HIM) with $T > 10^4 \text{ K}$ that is pressurized by the supernova feedback in star-forming regions, as we will describe later in Section 4.1. The mass of the cold gas with $T < 10^4 \text{ K}$ is then estimated with a sub-resolution ISM model as described in detail by Springel & Hernquist (2003a,b). In this sub-resolution ISM model, the hot and cold phase is assumed to be in pressure equilibrium (McKee & Ostriker 1977). The mass in high-density star-forming gas is dominated by the cold gas with $T < 10^4 \text{ K}$, and the volume is dominated by the hot component.

In the following sections, we will further supplement the simulation with a two-phase sub-resolution model in order to divide the cold gas with $T < 10^4 \text{ K}$ in the simulation into a cold neutral medium (CNM, with $T \sim 80 \text{ K}$ and $n \sim 10 \text{ cm}^{-3}$) and a warm neutral medium (WNM, with $T \sim 8000 \text{ K}$ and $n \sim 0.1 \text{ cm}^{-3}$). Therefore, in principle we are picturing a 3-phase medium with HIM, WNM, and CNM (cf. McKee & Ostriker 1977).

Within this multiphase ISM picture, Wolfire et al. (2003) estimated that the scale ℓ_P on which turbulent pressure begins to dominate the thermal pressure is $\sim 215 \text{ pc}$ for the WNM, based on the comparison of turbulent velocity dispersion and thermal velocity dispersion. Also the model of the vertical distribution of the H I by Dickey & Lockman (1990) suggests that the FWHM of the vertical gas distribution of the WNM is $\sim 500 \text{ pc}$ (Wolfire et al. 2003). These two estimates indicate that the volume occupied by the warm ionized medium and the WNM could be substantial compared to that of the HIM in an ISM with a scale $\sim 1 \text{ kpc}$. Furthermore recent high-resolution numerical simulations of a turbulent ISM suggest that the volume fraction of WNM could be comparable to that of HIM (Kritsuk & Norman

2002a,b; Kritsuk & Norman 2004). Since we are focusing on high-density ISM where the mass and density is dominated by the neutral component, here we restrict ourselves to the two-phase picture of the CNM and WNM, and in the following neglect the volume occupied by the HIM for the simplicity of the present sub-resolution model. Obviously this is an oversimplification of the actual 3-phase ISM, and could lead to an over-estimate of the volume fraction of CNM and thereby to an overestimate of the total [C II] emission of galaxies. Therefore, the predicted amount of CNM gas based on our simplified model is more likely to be an overestimate rather than an underestimate. By the construction of our model, the total amount of CNM determined in our simulation cannot exceed the total amount of cold neutral gas (with $T < 10^4$ K, i.e., CNM+WNM) given by the simulation.

3. The Model

In this section, we describe a simple analytic model to estimate the mass fraction of the CNM for given mean gas density, FUV radiation intensity, metallicity, and dust-to-gas ratio. The notation that we use hereafter in the paper is summarized in Table 2. As noted earlier, our work is largely motivated by that of Wolfe et al. (2003b). These authors recently opened a new window for probing star formation in high-redshift galaxies utilizing the C II* absorption line observed in DLAs. The idea is to use this absorption line to infer the cooling rate owing to the [C II] fine structure line, which in turn tells us about the heating rate caused by the FUV radiation field from nearby star formation. One can then estimate the projected star formation rate ($\dot{\psi}_\star$) in DLAs as the heating rate is expected to be proportional to the local star formation rate (SFR).

Wolfe et al. (2003b) considered a two-phase model in which the CNM and WNM are in pressure equilibrium. Subsequently Wolfe et al. (2003a) ruled out a solution in which C II* absorption arises in the WNM, as it overpredicts the observed bolometric extragalactic background radiation. Howk et al. (2005) showed directly that C II* absorption in one DLA cannot arise in the WNM. Since C II* absorption arises from the same $^2P_{3/2}$ state which gives rise to the [C II] emission, we assume that the CNM is the dominant source for the [C II] emission in this paper.

3.1. Set-up & Key Equations

Consider a ISM with mean density ρ_0 and volume V_0 in the vicinity of a star-forming region. This interstellar cloud consists of CNM and WNM that are in thermal equilibrium

within each cloud, and the two have density ρ_C and ρ_W , volume V_C and V_W , respectively. We also denote the volume fraction occupied by CNM by $f_V = V_C/V_0$, and the mass fraction of the CNM by f_M . Given these definitions, the following simple relations immediately follow:

$$\rho_C V_C + \rho_W V_W = \rho_0 V_0, \quad (\text{mass conservation}) \quad (1)$$

$$V_C + V_W = V_0, \quad (\text{volume conservation}) \quad (2)$$

$$f_M = \frac{\rho_C V_C}{\rho_0 V_0} = \frac{\rho_C}{\rho_0} f_V. \quad (3)$$

As mentioned above, in Equations (1) & (2), the volume of the HIM is ignored, and we are assuming that the volume fraction of the WNM is fairly substantial. Eliminating V_W from Equations (1) & (2) gives

$$f_V = \frac{V_C}{V_0} = \frac{\rho_0 - \rho_W}{\rho_C - \rho_W} = \frac{1 - (\rho_W/\rho_0)}{\left(\frac{\rho_C}{\rho_W} - 1\right) \frac{\rho_W}{\rho_0}}, \quad \text{and} \quad (4)$$

$$\rho_0 = (1 - f_V)\rho_W + f_V\rho_C. \quad (5)$$

Equation (5) can also be obtained from Equation (1) by dividing both sides by V_0 .

Combining equations (3), (4), & (5) gives

$$f_M = \frac{1}{\left(\frac{1-f_V}{f_V}\right) \left(\frac{\rho_W}{\rho_C}\right) + 1} = \frac{1 - (\rho_W/\rho_0)}{1 - (\rho_W/\rho_C)}. \quad (6)$$

Therefore, if we have estimates for ρ_C/ρ_W , and ρ_W/ρ_0 (or equivalently ρ_C/ρ_W , and f_V), then we can compute the mass fraction of the CNM using Equation (6). Note that knowing the volume fraction of the CNM, f_V , is equivalent to constraining the mean density ρ_0 if ρ_C and ρ_W are known, and the two quantities (f_V and ρ_0) are related to each other via Equation (4) or (5).

3.2. Phase Diagrams

In order to identify the CNM and WNM densities, we compute the two-phase structure of a multiphase ISM by solving the equations of thermal and ionization equilibrium for a given gas density, FUV radiation field intensity, metallicity, and dust-to-gas ratio with the numerical techniques and iterative procedures outlined in Wolfire et al. (1995) and Wolfe et al. (2003b). We describe the further details of our method in Appendix A.

Solving for the thermal balance results in a characteristic shape of pressure curves as a function of gas density as shown in the top panels of Figure 1 with a local minimum

($P = P_{\min}$) and maximum ($P = P_{\max}$) defined by $\partial(\log P)/\partial(\log n) = 0$. In this figure, the pressure curves are shown as a function of gas density for different input projected SFR per unit physical area ($\dot{\psi}_\star$) and metallicity ($\log(Z/Z_\odot)$). Our full grid of models covers the range $\log \dot{\psi}_\star [M_\odot \text{ yr}^{-1} \text{ kpc}^{-2}] = -4.0, -3.5, -3.0, -2.5, -2.0, -1.5, -1.0, -0.5$, & 0.0 , and $\log(Z/Z_\odot) = -2.5, -2.0, -1.5, -1.0, -0.5$, & 0.0 . Two things can be read off from this figure: (1) When $\dot{\psi}_\star = 0$ and only the UV background radiation is present, the resulting pressure curve appears almost identical to the case of $\log \dot{\psi}_\star = -4.0$; i.e., the impact of the UV background is negligible when $\log \dot{\psi}_\star \gg -4.0$. (2) As $\dot{\psi}_\star$ (or equivalently, the incident FUV radiation intensity) increases, the pressure maxima and minima move towards the upper right corner. For densities between those corresponding to P_{\max} and P_{\min} , the cooling curve is relatively insensitive to changes in temperature T . Therefore, at a given density, T undergoes a large increase when the cooling rate rises to match the increase in heating rate, thereby increasing the pressure. Conversely, outside this range in densities, the cooling curve increases rapidly with increasing T and as a result the pressure is insensitive to increases in heating rate. Also, as the metallicity decreases, metal-line cooling becomes inefficient, and the density and temperature have to be raised for a given heating rate, and therefore the equilibrium pressures go up.

It is known that the two thermally stable phases can coexist over a narrow range of pressures $P_{\min} < P < P_{\max}$, where $\partial(\log P)/\partial(\log n) > 0$. Here, we follow the work by Wolfire et al. (1995) and Wolfe et al. (2003b), and assume that the equilibrium gas pressure equals the geometric mean pressure $P = P_{\text{geo}} \equiv \sqrt{P_{\min} P_{\max}}$ for identifying ρ_C and ρ_W , as indicated by the open triangles in the phase diagrams shown in the top panels of Figure 1. In passing, we note that Kritsuk & Norman (2002a,b) have shown, using high resolution numerical simulations, that the thermally unstable turbulent ISM settles down as a multiphase medium, where the majority of the masses (for both CNM and WNM) lie close to the local minimum pressure P_{\min} .

For each equilibrium curve, the model of Wolfe et al. (2003b) gives the $[\text{C II}]$ luminosity per hydrogen atom, ℓ_c , as a function of gas density as we describe in Appendix A. The value of ℓ_c for the CNM can be determined at the CNM density as shown by the open triangles in the bottom panels of Figure 1. The value of ℓ_c increases with increasing metallicity as the heating of the gas (and correspondingly the cooling rate to match that) becomes more efficient via the grain photoelectric heating effect. At low metallicity (e.g., $\log(Z/Z_\odot) = -2.5$, the bottom left panel of Figure 1), the value of ℓ_c begins to decrease at high densities, because grain photoelectric heating becomes more inefficient owing to low dust content, and the heating becomes dominated by X-rays. The X-ray heating rate decreases with density since it becomes less efficient with increasing neutral gas fraction, which increases with density. In the case of $\log(Z/Z_\odot) = -0.5$, the value of ℓ_c continues to increase with increasing density as

the grain photoelectric heating remains efficient. The flattening of the curves at low density occurs when the cosmic microwave background (CMB) photons dominate the population rates of the fine-structure states. Note, the flattening is absent from the figure at very low metallicity since the population of the $^2P_{3/2}$ state is proportional to metallicity when the CMB dominates.

3.3. Mass fraction of CNM: f_M

Figures 2 and 3 illustrate the properties of our multiphase ISM model. Figure 2 shows ρ_C , ρ_W , the ratio of the two, and f_M as functions of projected SFR $\dot{\psi}_\star$ for different metallicities, while Figure 3 shows P_{\min} as a function of $\dot{\psi}_\star$ for different metallicities. Figures 2a, 2b, and 3 demonstrate that ρ_W , ρ_C , and P_{\min} are smooth monotonically increasing functions of $\dot{\psi}_\star$ as expected from Figure 1; as $\dot{\psi}_\star$ increases, the equilibrium pressure P_{geo} increases as does the equilibrium density. For a given $\dot{\psi}_\star$, as the metallicity decreases, the equilibrium density increases for cooling to match the heating rate. The CNM and WNM density scale roughly similarly, therefore the ratio ρ_W/ρ_C is relatively flat as a function of $\dot{\psi}_\star$ as shown in Figure 2c except for $\log(Z/Z_\odot) < -2.0$ and $\log \dot{\psi}_\star > -1.0$. As a result, f_M is a monotonically *decreasing* function of $\dot{\psi}_\star$. Here, the values of f_M were computed by Equation (6) assuming a constant value of $f_V = 7 \times 10^{-4}$, which is motivated by the following argument.

Consider a column of length L and a cross section of unit physical area through the ISM. Let f_A denote the area covering fraction of the CNM, and n_{cl} the number density of the CNM cloud, and R the physical radius of each CNM (spherical) cloud. Then,

$$f_V = \frac{4\pi}{3} R^3 n_{\text{cl}}, \quad \text{and} \quad (7)$$

$$f_A = \pi R^2 n_{\text{cl}} L. \quad (8)$$

Combining the above two equations and assuming typical values of $f_A \sim 0.5$, $L \sim 1$ kpc, and $R \sim 1$ pc gives

$$f_V = 1.33 f_A \frac{R}{L} \sim 1.33 \times 0.5 \times \frac{1 \text{ pc}}{1 \text{ kpc}} = 7 \times 10^{-4}, \quad \text{and} \quad (9)$$

$$n_{\text{cl}} = \frac{f_A}{\pi R^2 L} = 1.6 \times 10^{-4} \text{ pc}^{-3}. \quad (10)$$

We take $f_A \sim 0.5$ because Wolfe et al. (2003b) find CNM gas in roughly half of the observed DLAs. If we instead adopt $L = 100$ pc, then $f_V = 7 \times 10^{-3}$ and $n_{\text{cl}} = 1.6 \times 10^{-3} \text{ pc}^{-3}$, which are in better agreement with the values adopted by McKee & Ostriker (1977). However the latter values result in f_A greater than unity.

It is not surprising that the value of f_V is very small, as the volume occupied by CNM clouds should be much smaller than that of the WNM. If we take Equation (9) and compute the values of f_M using Equation (6), we obtain Figure 2d. The exact values of f_V and f_M are not important here, because when we later couple this model with cosmological simulations, we do *not* assume a constant value of f_V . Instead, we take the mean density of the ambient ISM ρ_0 directly from our hydrodynamic simulations and compute the value of f_M for each gas element in the simulation using Equation (6).

In summary, the procedure to obtain the CNM mass fraction in our model is as follows:

1. Compute a grid of equilibrium curves in the phase space of pressure and density for a range of projected star formation rates and metallicities (top panels of Figure 1).
2. For each equilibrium curve, identify ρ_C and ρ_W at $P_{\text{geo}} = \sqrt{P_{\text{min}} P_{\text{max}}}$.
3. Use Equation (6) and the inferred values of ρ_C and ρ_W to obtain f_M . Here we take the mean gas density ρ_0 directly from the result of cosmological simulations, and compute the amount of CNM gas for each dark matter halo as we show in Section 4.2. The model of Wolfe et al. (2003b) gives the [C II] luminosity per H atom ℓ_c as a function of $\dot{\psi}_*$ (see Appendix A), and we describe how we compute the [C II] luminosity of each halo in Section 4.3.

4. Results from Cosmological Simulations

4.1. Star-forming gas in simulations

Let us first look at the range of gas pressure and density that our cosmological hydro simulations cover. Figure 4 shows the distribution of cosmic gas in our cosmological simulations in the plane of density vs. pressure. In the simulation, the gas that has density higher than the threshold density $n_{\text{th}} = 0.13 \text{ cm}^{-3}$ is treated as a multiphase medium and is able to form stars, as described by the sub-resolution ISM model of Springel & Hernquist (2003a,b). We consider this star-forming gas as the ambient ISM (with mean density ρ_0) that hosts CNM and WNM. The magenta *dashed* curve to the right of the SF threshold density is the analytic fit to the effective equation of state adopted in the simulation (Robertson et al. 2004). *We stress that in Figure 4 we are plotting ρ_0 vs. P for the simulations.* The star-forming gas in the simulation is pressurized by heating owing to supernova feedback, and has a higher pressure than isothermal ($P \propto n$) gas as traced by the magenta *dashed* line. The Q5, D5, and G5 runs also include a treatment of feedback owing to galactic winds. In this approach, a fraction of supernova feedback energy is given to star-forming gas particles

as kinetic energy and momentum in random directions, and some gas particles are ejected from star-forming regions owing to winds. Therefore, one can see that the spread of the gas distribution around the effective equation-of-state is larger in the Q5, D5, and G5 runs than in the O3 (no wind) run. The distribution of gas in the Q5, D5, and G5 runs is roughly the same.

The three sets of two lines indicate the P_{\min} obtained from the pressure curves for metallicities of, from upper right to bottom left, $\log(Z/Z_{\odot}) = -2.5$ (black), -1.0 (blue), and 0.0 (red), as a function of ρ_C (the CNM density, shown in solid lines) and ρ_W (the WNM density, shown in *dot-dashed* lines) at P_{geo} , respectively. We stress again that in Figure 4 we are plotting ρ_0 vs. P for the simulations, whereas the analytic model calculation results show P vs. ρ_C and ρ_W . The criteria that we impose for the simulated gas to qualify for hosting CNM are $P > P_{\min}$ and $\rho_0 > \rho_W$ (see Equations [4] and [6]). The condition $\rho_C > \rho_W$ is guaranteed by the construction of the model.

The highest gas densities ρ_0 attained in our simulations are $n \sim 300 \text{ cm}^{-3}$ in the Q5 run, and $n \sim 100 \text{ cm}^{-3}$ in other runs. Most of the star-forming gas in the simulations has a higher pressure than P_{\min} in all runs, but we need to divide the gas into different metallicity ranges to perform a more detailed comparison.

In Figure 5, the gas in the Q5 run is divided into different metallicity ranges, and is compared to the corresponding values of P_{\min} for the same metallicity range. It is seen that most of the star-forming gas, i.e., gas with $n_{\text{th}} \geq 0.13 \text{ cm}^{-3}$, in the simulation is relatively metal-rich, and there is almost no star-forming gas with $\log(Z/Z_{\odot}) < -2.5$ that satisfies $P > P_{\min}$. Since the simulation does not resolve the high density CNM directly, it is not a problem that the diluted density of the simulated gas does not fall in-between the range $P_{\min} < P < P_{\max}$ for the CNM densities ρ_C .

4.2. CNM gas in dark matter halos

Before we compute the CNM mass in each dark matter halo, there are several steps in processing the simulation data. First, we identify dark matter halos by applying a conventional friends-of-friends algorithm to the dark matter particles in each simulation. After dark matter halos are identified, we set up a 3-dimensional cubic grid centered at the center of each dark matter halo covering the entire halo, with grid cell-size equal to the gravitational softening length of each simulation. Then, the gas mass, H I mass, metal mass, and star formation rate of each gas particle is smoothed over a spherical region of grid-cells, weighted by the SPH kernel. We now have all of the above quantities for each grid cell. These procedures

are the same as adopted by Nagamine et al. (2004b,c).

We now compute the CNM mass contained in each dark matter halo. Given the four quantities $(\rho_0, P, \psi_*, Z/Z_\odot)$ in each grid cell that covers the dark matter halo and the two quantities (ρ_C, ρ_W) obtained from the phase diagram shown in Figure 1, we can calculate the value of f_M for each grid cell using Equations (6). Here, only those cells that satisfy $P > P_{\min}$ and $\rho_0 > \rho_W$ (see Equations [4] and [6]) are considered to host CNM. Figure 6 shows the volume-averaged value of f_M for each halo, $\langle f_M \rangle$, where all the grid cells in each halo are equally averaged over and each point in this plot represents one halo. Contours are used to represent the scatter and avoid a saturation of points in the figure. The values of $\langle f_M \rangle$ are in the range $0.5 - 0.8$ for relatively massive halos with $M_{\text{halo}} > 10^{11} h^{-1} M_\odot$. The O3 run has higher values of $\langle f_M \rangle$ owing to the absence of winds. The rapid decline of $\langle f_M \rangle$ values at $10 < \log M_{\text{halo}} < 12$ for the D5 and G5 runs owes to lower resolution in simulations with large box sizes. We consider that a true physical decline of $\langle f_M \rangle$ should occur at $\log M_{\text{halo}} \sim 8.5$, because at this mass-scale the DLA cross section decreases rapidly in the highest resolution runs as shown in Figures 2 & 3 of Nagamine et al. (2004c), and hence the CNM mass fraction is expected to decrease as well.

Using the value of f_M computed for each grid cell that covers the dark matter halo, we calculate the total CNM mass of each halo according to

$$M_{\text{CNM}} = \sum_i f_M \rho_0 V_0, \quad (11)$$

where ρ_0 and V_0 are the gas density and the volume of each grid cell, and the index i runs through all grid cells for each halo. The resulting M_{CNM} for each halo is shown in Figure 7. The shaded contours are for the CNM, and the black contour without the shade is the total neutral hydrogen mass in the halo. As we described in Section 2, ionization equilibria of hydrogen and helium are solved assuming an optically thin limit across the simulation box. However, in high density star-forming regions, the recombination time-scales are expected to be shorter than the ionization time-scales, rendering some reliability in our estimate of the total neutral hydrogen mass in each halo (see Section 5 for the prospects of improving upon this in the future). The CNM mass in our model cannot exceed the black contour by construction. The *short-dashed*, *dash-dot*, *long-dashed* lines indicate the 5%, 1%, and 0.5% of the halo mass, respectively.

In the case of the O3 (no wind) run, the bulk of gas (both total neutral mass and the CNM mass) has mass fractions in-between 1 to 5% for most of the halos. These values are very close to that of the disk mass fraction 0.05 adopted by Mo et al. (1998). The most massive halos in the O3 run have slightly lower neutral mass fractions ($\sim 3\%$) than this value. When galactic wind feedback becomes strong (Q5, D5, and G5 runs), the total neutral mass fraction goes down to $\sim 1\%$, and the CNM mass fraction to even lower values ($0.1 - 1\%$).

This is because the gas is heated and ejected owing to winds, resulting in a lower neutral fraction. Similarly to Figure 6, the rapid decline of M_{CNM} values at $10 < \log M_{\text{halo}} < 12$ for D5 and G5 run owe to lower resolution in simulations with large box-sizes, and we consider that a true physical decline of M_{CNM} should also occur at $M_{\text{halo}} \sim 10^{8.5} h^{-1} M_{\odot}$.

4.3. [C II] emission from CNM

Having obtained the CNM mass of each grid cell computed in the previous section, we can now compute the [C II] luminosity of each halo by performing a similar sum to Equation (11) with an additional multiplication of [C II] luminosity per H atom, ℓ_c , as follows:

$$L_{\text{CII}} = \sum_i \ell_c(Z, \dot{\psi}_{\star}) \frac{f_M \rho_0 V_0}{\mu m_{\text{H}}}, \quad (12)$$

where μ is the mean molecular weight and m_{H} is the hydrogen mass. Notice that ℓ_c is a function of metallicity Z and $\dot{\psi}_{\star}$ of each grid cell. The resulting [C II] luminosity of each halo is shown in Figure 8. Each point in this diagram represents a halo, but we use contours in order to avoid saturation in the scatter plot. The *long-dashed* and *short-dashed* lines correspond to the following scaling relationships:

$$L_{\text{CII}} = C_1 \left(\frac{M_{\text{halo}}}{10^{12} h^{-1} M_{\odot}} \right), \quad (13)$$

where $C_1 = 10^{41}$ and $10^{40} \text{ erg s}^{-1}$, respectively. Most of the halos except for the least massive ones in the ‘no-wind’ (O3) run follow $C_1 = 10^{41} \text{ erg s}^{-1}$ well, and the ‘strong wind’ (Q5, D5, G5) runs are better characterized by $C_1 = 10^{40} \text{ erg s}^{-1}$. The decrease of L_{CII} in the least massive halos in each run occur owing to same reasons as mentioned for Figure 6.

Another way to characterize the distribution of [C II] luminosity of halos is to look at the cumulative luminosity function, which is shown in Figure 9. As expected from Figure 8, the ‘no-wind’ (O3) run is brighter than the ‘strong wind’ (Q5, D5, and G5) runs by about an order of magnitude. The bright-end of the O3 and Q5 run is limited by cosmic variance owing to small simulation box-sizes, and the faint-end of the D5 and G5 runs are limited by the low resolution in large box-size simulations. The total luminosity function can be obtained by interpolating the results of the three runs when they overlap. We will perform such interpolation in the next section and in Figure 12.

4.4. Comparison with LBG Luminosity Function

The connection between DLA galaxies and LBGs is of significant interest. The recent measurements of cross-correlation between DLAs and LBGs (Gawiser et al. 2001; Adelberger et al. 2003; Bouche & Lowenthal 2003, 2004; Cooke et al. 2006) suggest that the typical DLA halo mass could be similar to that of the LBGs’ ($M_{\text{halo}} \simeq 10^{12} M_{\odot}$), and that DLAs could be strongly correlated with LBGs. Since LBGs contribute a significant fraction of star formation rate density at $z \simeq 3$ and DLAs dominate the total H I gas density at the same redshift, it is natural to expect that the two systems have some connection with each other. In this case, the energy input source for the heating discussed in Section 3 would be the central LBGs in the halo rather than the *in situ* star formation within DLAs (Wolfe & Chen 2006).

In order to compare the computed [C II] luminosity function with the observed LBG population, we show in Figure 9 the observed number density of LBGs at $z = 3$ with magnitudes $R_{AB} < 25.5$ by Adelberger & Steidel (2000) and Adelberger et al. (2003) with a yellow shaded region. In addition, the following simple scaling laws and the observed cumulative luminosity function of LBGs can be used to obtain the magenta *dot-long-dashed* curve. Using the results of population synthesis calculations, Nagamine et al. (2005c) obtained a relationship between R_{AB} magnitude and halo mass M_{halo} as

$$R_{AB} = -2.5 \log M_{\text{halo}} + C_3, \quad (14)$$

where M_{halo} is in units of $h^{-1} M_{\odot}$ and $C_3 = 55.03$ (O3 run) and 57.03 (Q5 run). Inserting this equation into Equation (13) gives

$$\log L_{\text{CII}} = -0.4 (R_{AB} - C_3) + \log C_1 - 12. \quad (15)$$

For the case of the O3 run, this results in $\log L_{\text{CII}} = -0.4 R_{AB} + 51.01$. Next, we compute the cumulative luminosity function of LBGs using a Schechter fit with parameters $(m^*, \alpha, \Phi^*[h^3 \text{Mpc}^{-3}]) = (24.54, -1.57, 4.4 \times 10^{-3})$ obtained by Adelberger & Steidel (2000). We then convert the abscissa of this cumulative function using Equation (15) into [C II] luminosity. As a result, the two magenta *dot-long-dashed* curves in Figure 9 are obtained: the brighter one on the right is for the O3 run scaling, and the fainter one on the left is for the Q5 run scaling. We also indicate the magnitudes $R_{AB} = 23.5, 25.5, 30.0$, and 36.0 on this curve with filled triangles for the O3 run, which correspond to $\log L_{\text{CII}} = 41.61, 40.81, 39.01$, and 36.61 , respectively. The agreement between the two magenta curves and the actual simulation results is not perfect, but the two magenta curves lie in-between the ‘no-wind’ (O3) result and the ‘strong wind’ (Q5, D5, and G5) results, which we consider reasonable given the crudeness of the above scaling relationships.

4.5. [C II] flux density

The [C II] flux density of each halo can be computed by

$$S_\nu = \frac{(1+z)L_\nu}{4\pi d_L^2} = \frac{(1+z)}{4\pi d_L^2} \frac{L_{\text{CII}}}{\Delta\nu}, \quad (16)$$

where $\Delta\nu = \nu_{158}(v_c/c)\eta$ is the line width, $\nu_{158} = 1897 \text{ GHz}$ is the rest-frame frequency of the [C II] emission line, and v_c is the circular velocity of the dark matter halo at a radius of overdensity 200,

$$v_c \equiv \left(\frac{GM_{\text{halo}}}{R_{200}} \right)^{1/2} = \left[GM_{\text{halo}}^{2/3} \left(\frac{4\pi}{3} \bar{\rho} 200 \right)^{1/3} \right]^{1/2} \quad (17)$$

$$= 123.5 \left(\frac{M_{\text{halo}}}{10^{11} h^{-1} M_\odot} \right)^{1/3} \left(\frac{1+z}{4} \right)^{1/2} \text{ km s}^{-1}. \quad (18)$$

The parameter η relates the halo circular velocity to the velocity width of the line. In principle, there is a broad distribution of velocity width depending on the local dynamics and geometry of the line emitting gas, resulting in a large scatter of η . Haehnelt et al. (1998) showed that, for DLAs, the median of the velocity width distribution is roughly 60% of the virial velocity of the halo. Here we adopt $\eta = 0.6$ following their work. Obviously this is an over-simplification of complex gas dynamics, but for now we are satisfied with this simple treatment. In the future we will compute the line profiles directly using the full velocity information in the simulations and study this issue in greater detail.

Using the [C II] luminosity shown in Figure 8 and Equation (16), we obtain the [C II] flux density for each halo at $z = 3$ as shown in Figure 10. The distribution is roughly similar to that of [C II] luminosity vs. halo mass, and can be characterized by

$$S_\nu = C_2 \left(\frac{M_{\text{halo}}}{10^{12} h^{-1} M_\odot} \right)^{2/3}, \quad (19)$$

where $C_2 = 10^{-0.2} = 0.63 \text{ mJy}$ (black *long-dashed* line, for the O3 run) and $10^{-1.2} = 0.063 \text{ mJy}$ (red *short-dashed* line, for the Q5, D5, and G5 runs). The flux density follows the scaling $S_\nu \propto M_{\text{halo}}^{2/3}$, because $L_{\text{CII}} \propto M_{\text{halo}}$ and $\Delta\nu \propto v_c \propto M_{\text{halo}}^{1/3}$. We summarize these results in Figure 11. This figure shows the lowest limiting halo mass one can probe for a given flux density limit. The limiting halo mass is higher for the strong-feedback case than the no-feedback case, because the [C II] flux density is lower in the strong-feedback case for a given halo mass due to smaller amount of CNM mass. The dispersion around the scaling relationships were roughly estimated by eye to be $\sim \pm 0.5$ dex from Figure 10.

The cumulative flux density function is shown in Figure 12. Here, we combine the results of the Q5, D5, and G5 runs to cover the entire range of flux density as shown by the *black solid* line. The method for this interpolation is somewhat ad hoc, but the conclusion of this paper is not strongly affected by the details of this interpolation method. We simply require that the interpolated line (the ‘Combined’ result) smoothly connects the result of different runs. Similarly to the [C II] luminosity function, the runs with small box-sizes (Q5 and O3 runs) are limited at the bright-end owing to a lack of massive systems, and the run with large box-size is limited at the faint-end owing to a lack of low-mass systems caused by the limited resolution. The result of the O3 run is brighter than that of the Q5 run roughly by an order of magnitude. Figure 12 suggests that the number density of galaxies at $z = 3$ with flux density $S_\nu > 0.1$ mJy is about $2 \times 10^{-2} \text{ Mpc}^{-3}$ for the case of the ‘no-wind’ (O3) run, and $3 \times 10^{-4} \text{ Mpc}^{-3}$ for the ‘strong wind’ run (the ‘Combined’ result).

Like Figure 9, we show the observed number density of LBGs with magnitudes $R_{AB} < 25.5$ at $z = 3$ by Adelberger & Steidel (2000) and Adelberger et al. (2003) with the yellow shaded region. In addition, the two magenta *dot-long-dashed* curves are similarly obtained by using the same cumulative luminosity function of LBGs as in Figure 9. Inserting Equation (14) into Equation (19) gives

$$\log S_\nu = -0.27 (R_{AB} - C_3) + \log C_2 - 8. \quad (20)$$

For the case of the O3 run, this results in $\log S_\nu = -0.27 R_{AB} + 6.7$ (hereafter ‘O3-scaling’). We use this scaling and obtain the two magenta *dot-long-dashed* curves in Figure 12: the brighter one on the right is for the ‘O3-scaling’, and the fainter one on the left is for the ‘Q5-scaling’. We also indicate the magnitudes $R_{AB} = 23.5, 25.5, 30.0$, and 36.0 on this curve with filled triangles, which correspond to $S_\nu = 2.3, 0.7, 0.04$, and 9.5×10^{-4} mJy, respectively, for the ‘O3-scaling’ case. The curve for the ‘O3-scaling’ roughly agrees with the actual simulation result, but the ‘Q5-scaling’ curve is in-between the actual O3 and the ‘Combined’ results.

Finally we look at the cumulative probability distribution function as a function of [C II] flux density in Figure 13. The striking fact is that the fraction of the sources with $S_\nu > 0.1$ mJy is very small at $z = 3$, i.e., less than 5%. The fraction of LBGs brighter than $R_{AB} = 30$ mag is also about the same level. This is due to the large number of faint sources in the CDM universe, and it is simply a reflection of a steeply increasing number of dark matter halos with decreasing halo mass. Using the observed luminosity function basically gives the same result. The O3 run gives the most optimistic result in terms of the fraction of sources, which suggests that $\sim 30\%$ of all sources have $S_\nu > 0.01$ mJy at $z = 3$.

5. Discussion & Conclusions

We have coupled state-of-the-art cosmological SPH simulations with an analytic model of a multiphase ISM in order to compute the [C II] emission from galaxies at $z = 3$. We find that, in a Λ CDM universe, the majority of the sources are very faint with $S_\nu < 0.1$ mJy. This is presumably a generic prediction of the CDM model owing to an increasing number of low-mass dark matter halos with decreasing halo mass. If our model prediction on the faintness of the [C II] sources is indeed correct, then it will be difficult for ALMA and SPICA to detect normal (i.e., not quasars, active AGNs, or strong submillimeter sources) high-redshift galaxies via [C II] emission in large number, as the sensitivity limit of both telescopes are expected to be $S_\nu \sim 0.1 - 1$ mJy. The recommended observing strategy is therefore to focus on very bright LBGs with $R_{AB} \lesssim 24$ mag that are pre-selected through optical imaging and spectroscopically known redshifts. Since there is a large body of spectroscopic data on LBGs at $z \gtrsim 3$, it should not be a problem to come up with observing targets. Our calculation shows that the brightest LBGs with $R_{AB} \sim 23.5$ mag could have flux densities $S_\nu = 1 - 3$ mJy depending on the strength of galactic wind feedback.

Some caveats to note for the present work is that we have assumed that the physical conditions of neutral gas in DLAs and LBGs are the same, and that the dust-to-gas ratios of the gas are similar. If these assumptions are inappropriate for the LBGs at $z \sim 3$, then the above conclusions might not be entirely accurate. Our multiphase ISM model also assumed the SMC-type (silicates) dust composition which is less efficient for heating than other models such as the Galactic (carbonaceous) or the LMC-type models of dust grains. The true nature of dust in DLAs could be different from what we assumed here, and we expect a factor of two uncertainty in the dust-to-gas ratio. Note, however, that the metallicity of LBGs approaches solar, which is significantly higher than for DLAs. As a result, it is natural to expect that gas surrounding LBGs would have a dust-to-gas ratio higher than for the average DLA. Since the heating rate of the gas is proportional to dust-to-gas ratio, the [C II] emission from LBGs is likely to be at the upper end of our calculation. In passing we note that star-forming DRG/BzK galaxies (van Dokkum et al. 2004; Daddi et al. 2004) would also be good candidates for [C II] observation as they are considered to have higher star formation rates and dust content than LBGs and hence more luminous in [C II] luminosity. But their space density is lower by a factor of ~ 10 than that of LBGs.

We have some confidence on the reliability of the properties of bright galaxies in the simulation, because we know from our previous work (Nagamine et al. 2004d; Night et al. 2006; Finlator et al. 2006) that the simulations can reproduce the observed properties of LBGs at $z = 3 - 6$ relatively well. However the neutral gas is not well resolved near the resolution limit of each simulation, and this introduces some uncertainty for low-mass

galaxies (except for the Q5 run in which low-mass galaxies are well modeled). For this reason our scaling laws were mainly determined using the data for the massive galaxies in the simulation. There is also an intrinsic scatter in the CNM mass as a function of halo mass around the scaling relation (Figure 7). As a result, we expect 30% uncertainty in our predictions of the CNM mass fractions for high-mass halos, and somewhat larger uncertainties for lower mass halos.

Even if the observation of normal high-redshift galaxies is difficult, the reward of [C II] detection from such galaxies would be quite significant, because such measurements would directly constrain the amount of neutral gas and the properties of ambient ISM in high-redshift galaxies which is otherwise difficult to do. The observations of DLAs (e.g. Prochaska et al. 2005; Wolfe et al. 2005) have given us tremendous insights on the properties of neutral gas in high-redshift galaxies already, but [C II] measurements will provide complementary information to further constrain theoretical/numerical models of galaxy formation. The combination of interferometric maps and the velocity widths of the [C II] emission could in principle tell us about the physical sizes of DLAs and the mass of hosting dark matter halos, as well as the physical properties of the gas such as the heating rate.

This paper is just a first step towards such a goal, and a number of improvements in the analysis are needed in the future. For example, in the current simulations, an optically thin approximation was assumed throughout when solving for ionization equilibrium, and a simple radiative transfer calculation assuming a disk geometry was used to approximate the effect of radiative transfer from local star-forming regions. As computing power increases, a more accurate treatment of radiative transfer (e.g., Razoumov et al. 2005) and ISM physics on small-scales will become possible using direct information from simulations, such as star formation rates and metallicity of the gas.

We acknowledge the significant contribution of Volker Springel to the simulations used in this work, and we thank for his useful comments on the manuscript. We are also grateful to Alexei Kritsuk for useful suggestions and discussions. This work was supported in part by NSF grants ACI 96-19019, AST 00-71019, AST 02-06299, and AST 03-07690, and NASA ATP grants NAG5-12140, NAG5-13292, and NAG5-13381. The simulations were performed at the Center for Parallel Astrophysical Computing at the Harvard-Smithsonian Center for Astrophysics.

A. Appendix: Details of the multi-phase ISM model

Here, we briefly summarize the multi-phase ISM model developed by Wolfe et al. (2003b). The model is used for the calculation of Figure 1 in this paper.

First, in order to relate the projected SFR per unit physical area, $\dot{\psi}_\star$, with the incident FUV radiation field J_ν , Wolfe et al. (2003b) assumed a plane parallel disk geometry with half-width h and radius R , in which the gas, dust, and stars are uniformly distributed. A disk is a reasonable approximation for dissipatively collapsing gas inside a dark matter halo, and it is also motivated by the observations of DLAs at $z \sim 3$ (e.g. Prochaska & Wolfe 1997, 1998). In the cosmological simulations used in this paper, we still lack the numerical resolution (and/or necessary physics) to properly account for the formation of disk galaxies in correct number, which is known as the ‘angular momentum problem’ (Robertson et al. 2004, and references therein). By assuming a disk geometry for the ISM model, we are implicitly assuming that the simulated galaxies also have the same geometry, which is a reasonable assumption.

A radiative transfer calculation under this geometry gives

$$J_\nu = \frac{1}{2} \left(\frac{\Sigma_\nu}{4\pi} \right) \left[1 + \ln \left(\frac{R}{h} \right) - k_\nu R \right] + O(k_\nu R)^2 \dots \quad (\text{A1})$$

when $k_\nu h \ll k_\nu R \ll 1$. The quantity Σ_ν is the luminosity per unit area on the surface of the disk, and k_ν is the absorption opacity of dust at frequency ν . This equation shows that J_ν depends on the aspect-ratio R/h only weakly. The relation $\Sigma_\nu = 8.4 \times 10^{-16} (\dot{\psi}_\star / M_\odot \text{ yr}^{-1} \text{ kpc}^{-2}) [\text{erg cm}^{-2} \text{ s}^{-1} \text{ Hz}^{-1}]$ is adopted from Madau & Pozzetti (2000). The effect of the UV background radiation is included in Σ_ν , but its effect is negligible compared to that owing to local star formation.

Once the relationship between J_ν and $\dot{\psi}_\star$ is obtained, we then compute the total heating rate Γ for a given value of $\dot{\psi}_\star$ as follows:

$$\Gamma = \Gamma_d + \Gamma_{\text{CR}} + \Gamma_{\text{XR}} + \Gamma_{\text{CI}}, \quad (\text{A2})$$

where the terms on the right-hand-side (RHS) are the heating rates owing to the grain photoelectric effect, cosmic rays, X-rays, and photoionization of C I by the FUV radiation field J_ν . In particular, the grain photoelectric heating rate per H atom, Γ_d , is related to $\dot{\psi}_\star$ as

$$\Gamma_d \propto \kappa \epsilon J_\nu [\text{erg s}^{-1} \text{ H}^{-1}] \propto \Sigma_\nu \propto \dot{\psi}_\star, \quad (\text{A3})$$

where κ is the dust-to-gas ratio and ϵ is the fraction of FUV radiation absorbed by grains and converted to gas heating (i.e., heating efficiency). The Γ_d was computed by adopting

the Weingartner & Draine (2001) expression for photoelectric efficiency in the case of pure silicates, blackbody FUV radiation, and extinction $R_V = 3.1$. The heating rates Γ_{CR} and Γ_{XR} are also assumed to be proportional to $\dot{\psi}_\star$.

The above heating rate has to be balanced with the total cooling rate Λ which includes the following terms:

$$\Lambda = \Lambda_{\text{FS}} + \Lambda_{\text{MS}} + \Lambda_{\text{Ly}\alpha} + \Lambda_{\text{GR}}, \quad (\text{A4})$$

where the first term on the RHS is the cooling rate owing to fine-structure lines of [C II] $158\,\mu\text{m}$ (which dominates at $T < 300\,\text{K}$) and [O I] $63\,\mu\text{m}$ (which is comparable to [C II] at $T > 300\,\text{K}$), i.e., $\Lambda_{\text{FS}} = \Lambda_{\text{CII}} + \Lambda_{\text{OI}}$. The second term on the RHS owes to metastable excitations of C^+ , O^0 , Si^+ , and S^+ , which becomes important at $T > 3000\,\text{K}$. The third and fourth term are the cooling by Ly α and grain recombination which become important at high temperatures. Cooling owing to transitions in the neutral species C^0 , Fe^0 , Mg^0 , and Si^0 are not included as their contribution to Λ is negligible.

We then let

$$\Gamma = n \Lambda \quad (\text{A5})$$

and solve the thermal and ionization equilibrium for given gas density n , dust-to-gas ratio, metallicity, and projected SFR. This leads to the two-phase gas structure as shown in the pressure curves in Figure 1. Once the thermal balance is achieved and CNM/WNM densities are identified, the [C II] emission per H atom can be obtained as

$$\ell_c = n \Lambda_{\text{CII}} + \ell_c^{\text{CMB}}, \quad (\text{A6})$$

where the latter term on the RHS is the spontaneous energy emission rate in the limit of CMB excitation. The quantity ℓ_c is shown in the bottom panels of Figure 1 as a function of density.

REFERENCES

- Adelberger, K. L. & Steidel, C. C. 2000, *ApJ*, 544, 218
- Adelberger, K. L., Steidel, C. C., Shapley, A. E., & Pettini, M. 2003, *ApJ*, 584, 45
- Beelen, A., Cox, P., Pety, J., Carilli, C. L., Bertoldi, F., Momjian, E., Omont, A., Petitjean, P., & Petric, A. O. 2004, *A&A*, 423, 441
- Blumenthal, G. R., Faber, S. M., Primack, J. R., & Rees, M. J. 1984, *Nature*, 311, 517
- Bouche, N. & Lowenthal, J. D. 2003, *ApJ*, 596, 810

—. 2004, *ApJ*, 609, 513

Carilli, C., Bertoldi, F., Omont, A., Cox, P., McMahon, R. G., & Isaak, K. G. 2001, *AJ*, 122, 1679

Carilli, C., Walter, F., Bertoldi, F., Menten, K. M., Fan, X., Lewis, G. F., Strauss, M. A., Cox, P., et al. 2004, *AJ*, 128, 997

Carral, P., Hollenbach, D. J., Lord, S. D., Colgan, S. W. J., Haas, M. R., Rubin, R. H., & Erickson, E. F. 1994, *ApJ*, 423, 223

Contursi, A., Kaufman, M. J., Helou, G., Hollenbach, D. J., et al. 2002, *AJ*, 124, 751

Cooke, J., Wolfe, A. M., Gawiser, E., & Prochaska, J. X. 2006, *ApJ*, 636, L9

Crawford, M. K., Genzel, R., Townes, C. H., & Watson, D. M. 1985, *ApJ*, 291, 755

Daddi, E., Cimatti, A., Renzini, A., Fontana, A., Mignoli, M., Pozzetti, L., Tozzi, P., & Zamorani, G. 2004, *ApJ*, 617, 746

Dalgarno, A. & McCray, R. 1972, *ARA&A*, 10, 375

Davé, R., Hernquist, L., Katz, N., & Weinberg, D. H. 1999, *ApJ*, 511, 521

Davis, M., Efstathiou, G., Frenk, C. S., & White, S. D. M. 1985, *ApJ*, 292, 371

Di Matteo, T., Springel, V., & Hernquist, L. 2005, *Nature*, 433, 604

Dickey, J. M. & Lockman, F. J. 1990, *ARA&A*, 28, 215

Finlator, K., Davé, R., Papovich, C., & Hernquist, L. 2006, *ApJ*, 639, 672

Furlanetto, S. R., Schaye, J., Springel, V., & Hernquist, L. 2003, *ApJ*, 599, L1

—. 2004, *ApJ*, 606, 221

—. 2005, *ApJ*, 622, 7

Gawiser, E., Wolfe, A. M., Prochaska, J. X., Lanzetta, K. M., Yahata, N., & Quirrenbach, A. 2001, *ApJ*, 562, 628

Haardt, F. & Madau, P. 1996, *ApJ*, 461, 20

Haehnelt, M., Steinmetz, M., & Rauch, M. 1998, *ApJ*, 495, 647

- Hopkins, P. F., Hernquist, L., Cox, T. J., Di Matteo, T., Robertson, B., & Springel, V. 2005, *ApJ*, in press (astro-ph/0506398)
- Howk, J. C., Wolfe, A. M., & Prochaska, J. X. 2005, *ApJ*, 622, L81
- Iwata, I., Ohta, K., Tamura, N., Ando, M., Wada, S., Watanabe, C., Akiyama, M., & Aoki, K. 2003, *PASJ*, 55, 415
- Kritsuk, A. G. & Norman, M. L. 2002a, *ApJ*, 569, L127
- . 2002b, *ApJ*, 580, L51
- Kritsuk, A. G. & Norman, M. L. 2004, *ApJ*, 601, L55
- Lanzetta, K. M., Wolfe, A. M., & Turnshek, D. A. 1995, *ApJ*, 440, 435
- Leech, K. J., Völk, H. J., Heinrichsen, I., Hippelein, H., Metcalfe, L., Pierini, D., Popescu, C. C., Tuffs, R. J., & Xu, C. 1999, *MNRAS*, 310, 317
- Lehner, N., Wakker, B. P., & Savage, B. D. 2004, *ApJ*, 615, 767
- Loeb, A. 1993, *ApJ*, 404, L37
- Madau, P. & Pozzetti, L. 2000, *MNRAS*, 312, L9
- Madden, S. C., Geis, N., Genzel, R., Herrmann, F., Jackson, J., Poglitsch, A., Stacey, G. J., & Townes, C. H. 1993, *ApJ*, 407, 579
- Maiolino, R., Cox, P., Caselli, P., Beelen, A., Bertoldi, F., Carilli, C. L., Kaufman, M. J., Menten, K. M., et al. 2005, *A&A*, 440, L51
- Malhotra, S., Helou, G., Stacey, G., Hollenbach, D., Lord, S., Beichman, C. A., Dinerstein, H., & Hunter, D. A. 1997, *ApJ*, 491, L27
- Malhotra, S., Kaufman, M. J., Hollenbach, D., Helou, G., Rubin, R. H., Brauher, J., Dale, D., Lu, N. Y., et al. 2001, *ApJ*, 561, 766
- McKee, C. F. & Ostriker, J. P. 1977, *ApJ*, 218, 148
- Mo, H. J. & Fukugita, M. 1996, *ApJ*, 467, L9
- Mo, H. J., Mao, S., & White, S. D. M. 1998, *MNRAS*, 295, 319
- Nagamine, K. 2002, *ApJ*, 564, 73

- Nagamine, K., Cen, R., Hernquist, L., Ostriker, J. P., & Springel, V. 2004a, *ApJ*, 610, 45
- . 2005a, *ApJ*, 627, 608
- . 2005b, *ApJ*, 618, 23
- Nagamine, K., Springel, V., & Hernquist, L. 2004b, *MNRAS*, 348, 421
- . 2004c, *MNRAS*, 348, 435
- Nagamine, K., Springel, V., Hernquist, L., & Machacek, M. 2004d, *MNRAS*, 350, 385
- Nagamine, K., Wolfe, A. M., Hernquist, L., & Springel, V. 2005c, *ApJ*, submitted (astro-ph/0510729)
- Night, C., Nagamine, K., Springel, V., & Hernquist, L. 2006, *MNRAS*, 366, 705
- Omont, A., Beelen, A., Bertoldi, F., & others et al. 2003, *A&A*, 398, 857
- Omont, A., Cox, P., Bertoldi, F., McMahon, R. G., Carilli, C., & Isaak, K. G. 2001, *A&A*, 374, 371
- Omont, A., McMahon, R. G., Cox, P., Kreysa, E., Bergeron, J., Pajot, F., & Storrie-Lombardi, L. J. 1996, *A&A*, 315, 1
- Ouchi, M., Shimasaku, K., Furusawa, H., Miyazaki, M., Doi, M., Hamabe, M., Hayashino, T., Kimura, M., et al. 2004a, *ApJ*, 611, 660
- Ouchi, M., Shimasaku, K., Okamura, S., Furusawa, H., Kashikawa, N., Ota, K., Doi, M., Hamabe, M., et al. 2004b, *ApJ*, 611, 685
- Petrosian, V., Bahcall, J. N., & Salpeter, E. E. 1969, *ApJ*, 155, L57+
- Pierini, D., Leech, K. J., Tuffs, R. J., & Volk, H. J. 1999, *MNRAS*, 303, L29
- Pierini, D., Lequeux, J., Boselli, A., Leech, K. J., & Völk, H. J. 2001, *A&A*, 373, 827
- Prochaska, J. X. & Herbert-Fort, S. 2004, *PASP*, 116, 622
- Prochaska, J. X., Herbert-Fort, S., & Wolfe, A. M. 2005, *ApJ*, submitted
- Prochaska, J. X. & Wolfe, A. M. 1997, *ApJ*, 487, 73
- . 1998, *ApJ*, 507, 113

- Razoumov, A. O., Norman, M. L., Prochaska, J. X., & Wolfe, A. M. 2005, *ApJ*, submitted (astro-ph/0510786)
- Robertson, B. E., Yoshida, N., Springel, V., & Hernquist, L. 2004, *ApJ*, 606, 32
- Russell, R. W., Melnick, G., Gull, G. E., & Harwit, M. 1980, *ApJ*, 240, L99
- Sauty, S., Gerin, M., & Casoli, F. 1998, *A&A*, 339, 19
- Shapley, A. E., Steidel, C. C., Adelberger, K. L., Dickinson, M., Giavalisco, M., & Pettini, M. 2001, *ApJ*, 562, 95
- Springel, V. 2005, *MNRAS*, 364, 1105
- Springel, V., Di Matteo, T., & Hernquist, L. 2005a, *ApJ*, 620, L79
- . 2005b, *MNRAS*, 361, 776
- Springel, V. & Hernquist, L. 2002, *MNRAS*, 333, 649
- . 2003a, *MNRAS*, 339, 289
- . 2003b, *MNRAS*, 339, 312
- Stacey, G. J., Geis, N., ad J. B. Lugten, R. G., Poglitsch, A., Sternberg, A., & Townes, C. H. 1991, *ApJ*, 373, 423
- Stark, A. A. 1997, *ApJ*, 481, 587
- Steidel, C. C., Adelberger, K. L., Adelberger, K. L., Shapley, A. E., Pettini, M., Dickinson, M., & Giavalisco, M. 2003, *ApJ*, 592, 728
- Steidel, C. C., Adelberger, K. L., Giavalisco, M., Dickinson, M., & Pettini, M. 1999, *ApJ*, 519, 1
- Storrie-Lombardi, L. J. & Wolfe, A. M. 2000, *ApJ*, 543, 552
- Suginohara, M., Suginohara, T., & Spergel, D. N. 1999, *ApJ*, 512, 547
- Tielens, A. G. G. M. & Hollenbach, D. 1985, *ApJ*, 291, 722
- van Dokkum, P., Franx, M., Schreiber, N. F., Illingworth, G., Daddi, E., Knudsen, K. K., Labbe, I., Moorwood, A., et al. 2004, *ApJ*, 611, 703
- Walter, F., Bertoldi, F., Carilli, C., Cox, P., Pierre, L. K. Y., Neri, R., Fan, X., Omont, A., et al. 2003, *Nature*, 424, 406

- Weinberg, D. H., Hernquist, L., & Katz, N. 2002, *ApJ*, 571, 15
- Weingartner, J. C. & Draine, B. T. 2001, *ApJS*, 134, 263
- Wolfe, A. M. & Chen, H.-W. 2006, *ApJ*, submitted
- Wolfe, A. M., Gawiser, E., & Prochaska, J. X. 2003a, *ApJ*, 593, 235
- . 2005, *ARA&A*, 43, 861
- Wolfe, A. M., Prochaska, J. X., & Gawiser, E. 2003b, *ApJ*, 593, 215
- Wolfe, A. M., Turnshek, D. A., Smith, H. E., & Cohen, R. S. 1986, *ApJS*, 61, 249
- Wolfire, M. G., Hollenbach, D., McKee, C. F., et al. 1995, *ApJ*, 443, 152
- Wolfire, M. G., McKee, C. F., Hollenbach, D., & Tielens, A. G. G. M. 2003, *ApJ*, 587, 278

Table 1. Simulation Parameters

Run	Box-size	N_p	m_{DM}	m_{gas}	ϵ	wind
O3	10.00	2×144^3	2.42×10^7	3.72×10^6	2.78	none
P3	10.00	2×144^3	2.42×10^7	3.72×10^6	2.78	weak
Q3	10.00	2×144^3	2.42×10^7	3.72×10^6	2.78	strong
Q5	10.00	2×324^3	2.12×10^6	3.26×10^5	1.23	strong
D5	33.75	2×324^3	8.15×10^7	1.26×10^7	4.17	strong
G5	100.0	2×324^3	2.12×10^9	3.26×10^8	8.00	strong

Note. — Simulations employed in this study. The box-size is given in units of $h^{-1} \text{Mpc}$, N_p is the particle number of dark matter and gas (hence $\times 2$), m_{DM} and m_{gas} are the masses of dark matter and gas particles in units of $h^{-1} M_{\odot}$, respectively, ϵ is the comoving gravitational softening length in units of $h^{-1} \text{kpc}$.

Table 2. Notation of Variables

Variable	Definition
ρ_C, ρ_W	density of CNM and WNM
ρ_0	mean density of the total gas
V_C, V_W	volume occupied by CNM and WNM
V_0	volume of the star-forming region under consideration
f_M	mass fraction of CNM
f_V	volume fraction of CNM
f_A	area covering fraction of CNM clouds
n_{cl}	number density of CNM clouds
R	characteristic radius of the spherical CNM cloud
L	size of the star-forming region

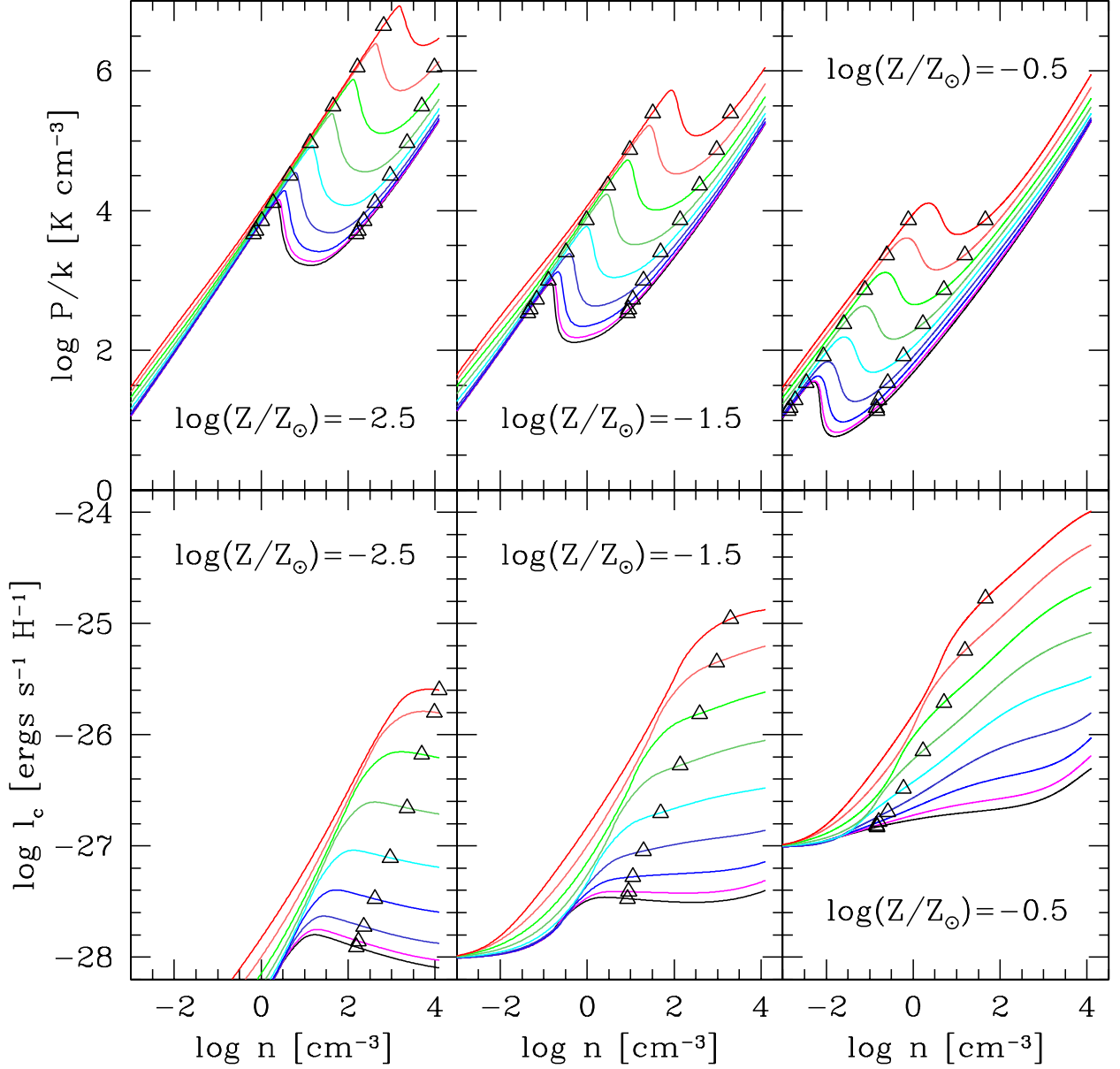


Fig. 1.— *Top panels*: Phase diagram of pressure vs. density for different projected SFR of $\log \dot{\psi}_* [M_\odot \text{ yr}^{-1} \text{ kpc}^{-2}] = -4.0, -3.5, -3.0, -2.5, -2.0, -1.5, -1.0, -0.5$, and 0.0 , from bottom (black) to top (red). The open triangles indicate the CNM and WNM densities at the geometric mean pressure $P_{\text{geo}} = \sqrt{P_{\text{max}} P_{\text{min}}}$. *Bottom panels*: [CII] luminosity per H atom, ℓ_c , as computed by the model of Wolfe et al. (2003b, see Appendix A). See text for the qualitative trends of the curves shown in this figure.

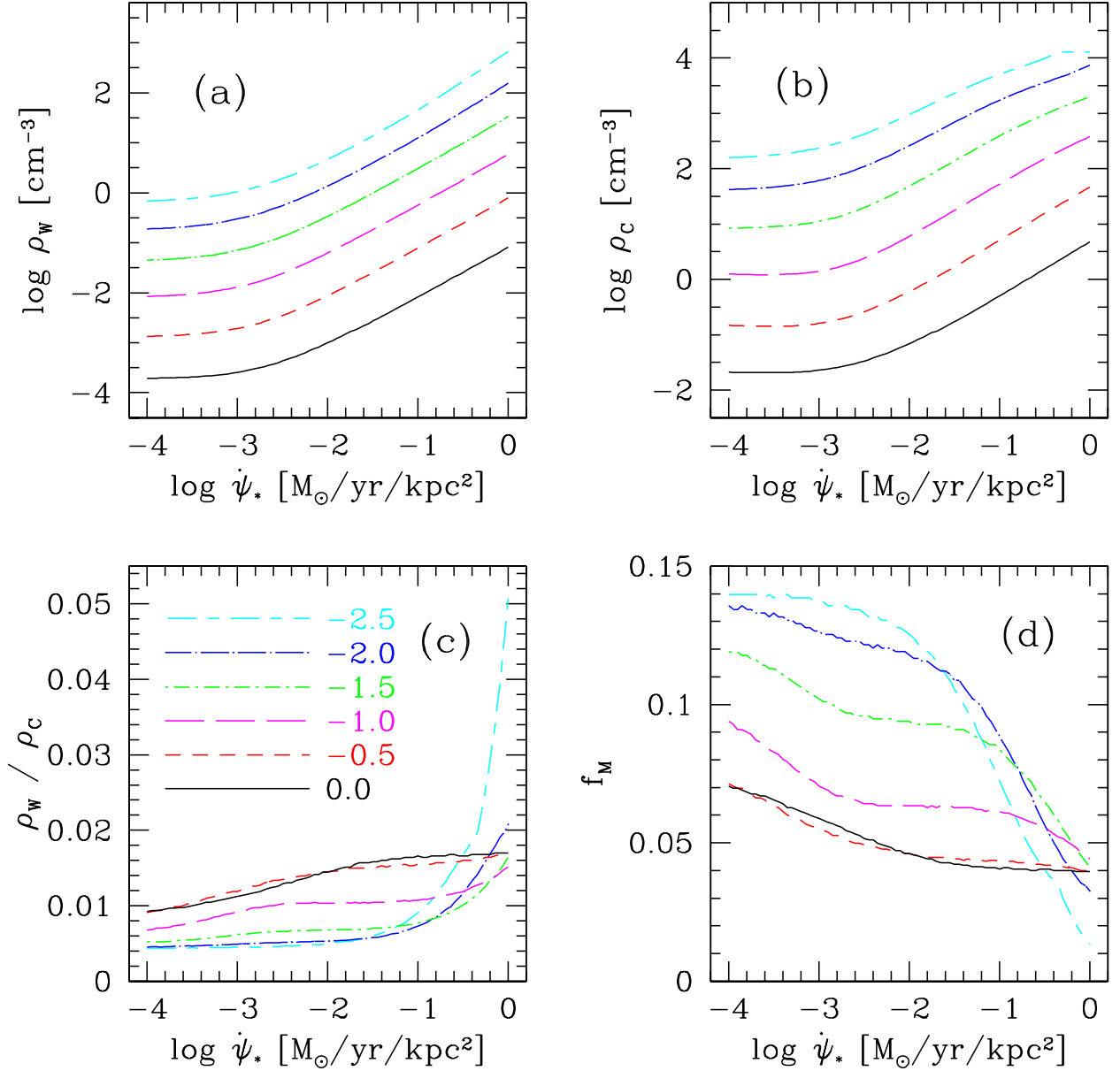


Fig. 2.— Following quantities are shown as a function of projected SFR per unit physical area ($\dot{\psi}_*$ [M_⊙ yr⁻¹ kpc⁻²]): WNM density ($\log \rho_W$, panel [a]), CNM density ($\log \rho_C$, panel [b]), the ratio of the two (ρ_W/ρ_C , panel [c]), and the mass fraction of CNM (f_M , panel [d]) as computed by Equation (6) assuming a constant value of $f_V = 7 \times 10^{-4}$ (see text). Different line types are for different metallicity as indicated in the legend of panel (c): $\log(Z/Z_\odot) = -2.5$ (long-dash short-dash), -2.0 (long dashed-dot line), -1.5 (short dash-dot), -1.0 (long dashed), -0.5 (short dashed), and 0.0 (solid).

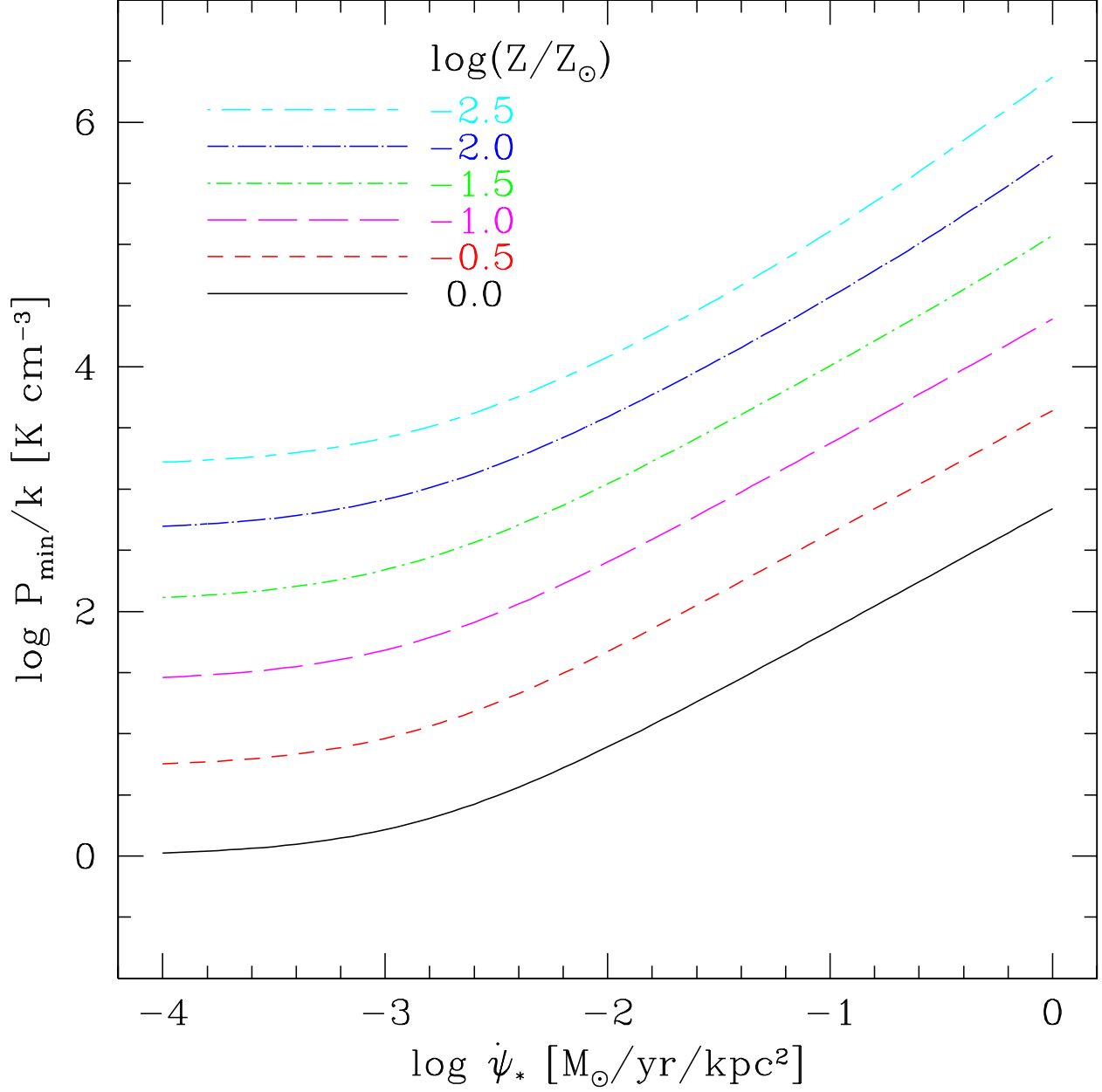


Fig. 3.— Projected SFR $\dot{\psi}_*$ vs. minimum pressure P_{min} described in Section 3.2 and 3.3. Different line types are for different metallicities as indicated in the legend. The simulated gas is required to satisfy $P > P_{\text{min}}$ and $\rho_0 > \rho_W$ in order to host the CNM gas.

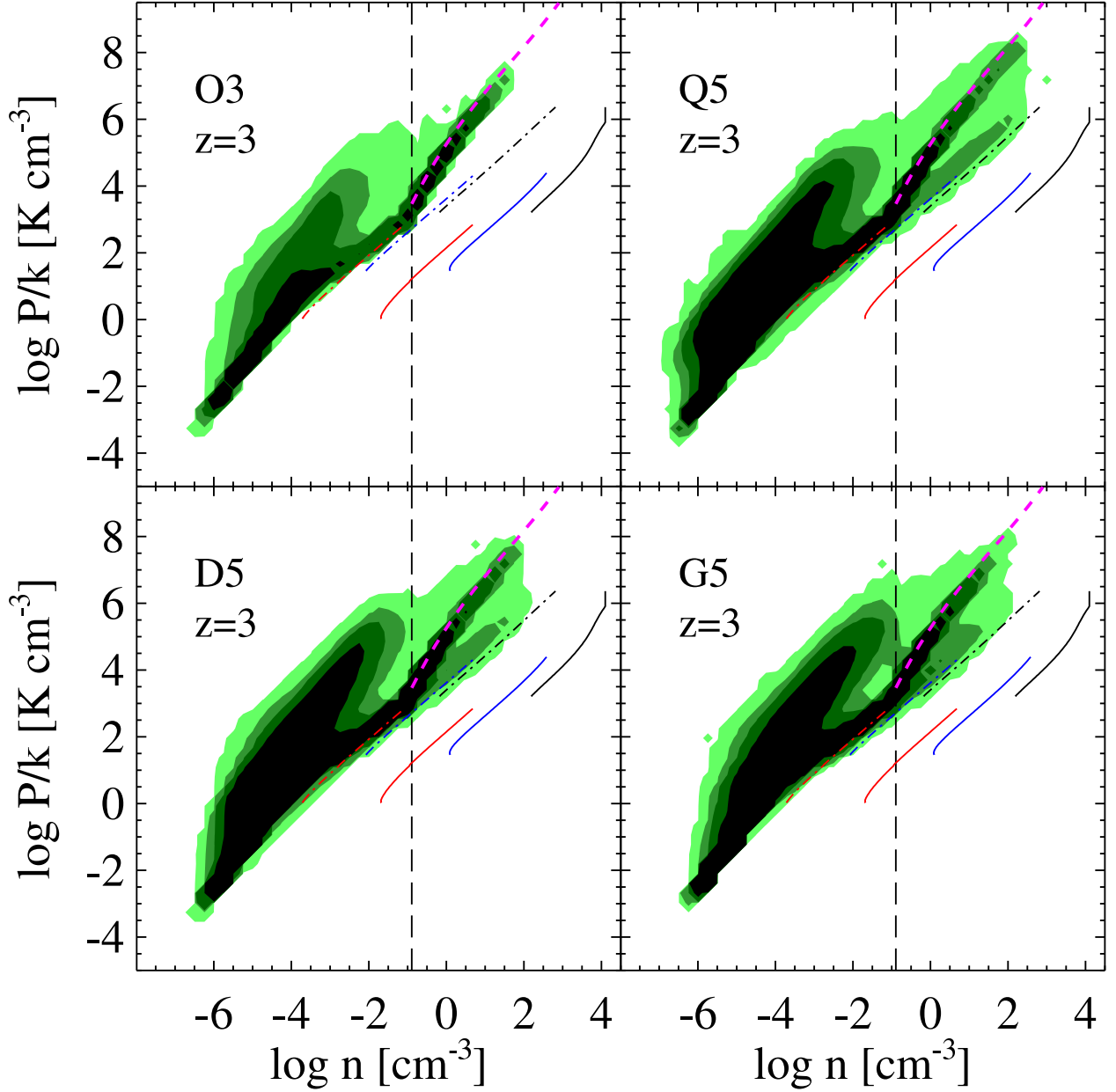


Fig. 4.— Density vs. pressure of all cosmic gas in our O3, Q5, D5, and G5 simulations at $z = 3$. The vertical dashed line indicates the threshold density $n_{\text{th}} = 0.13 \text{ cm}^{-3}$ for star formation to take place in the simulation, and the gas to the right-ward of this threshold density is treated as ambient gas in star-forming regions in which the CNM and WNM are hosted. The 3 sets of 2 lines indicate the P_{\min} for metallicities of $\log(Z/Z_{\odot}) = -2.5$ (black), -1.0 (blue), and 0.0 (red) as functions of WNM (*dot-dashed lines*) and CNM (*solid lines*) density at P_{geo} from upper right to bottom left, respectively. The lines for the WNM densities are shown because the criteria that we impose for the simulated gas to qualify for hosting CNM are $P > P_{\min}$ and $\rho_0 > \rho_w$ (see Equations [4] and [6]). The magenta dashed line is the analytic fit to the effective equation of state adopted in the simulation (Robertson et al. 2004). The 4 contour levels are for (1, 10, 100, 1000) gas particles in each 2-dimensional bin of size $(\Delta \log n, \Delta \log P/k) = (0.25, 0.29)$ from low to high level.

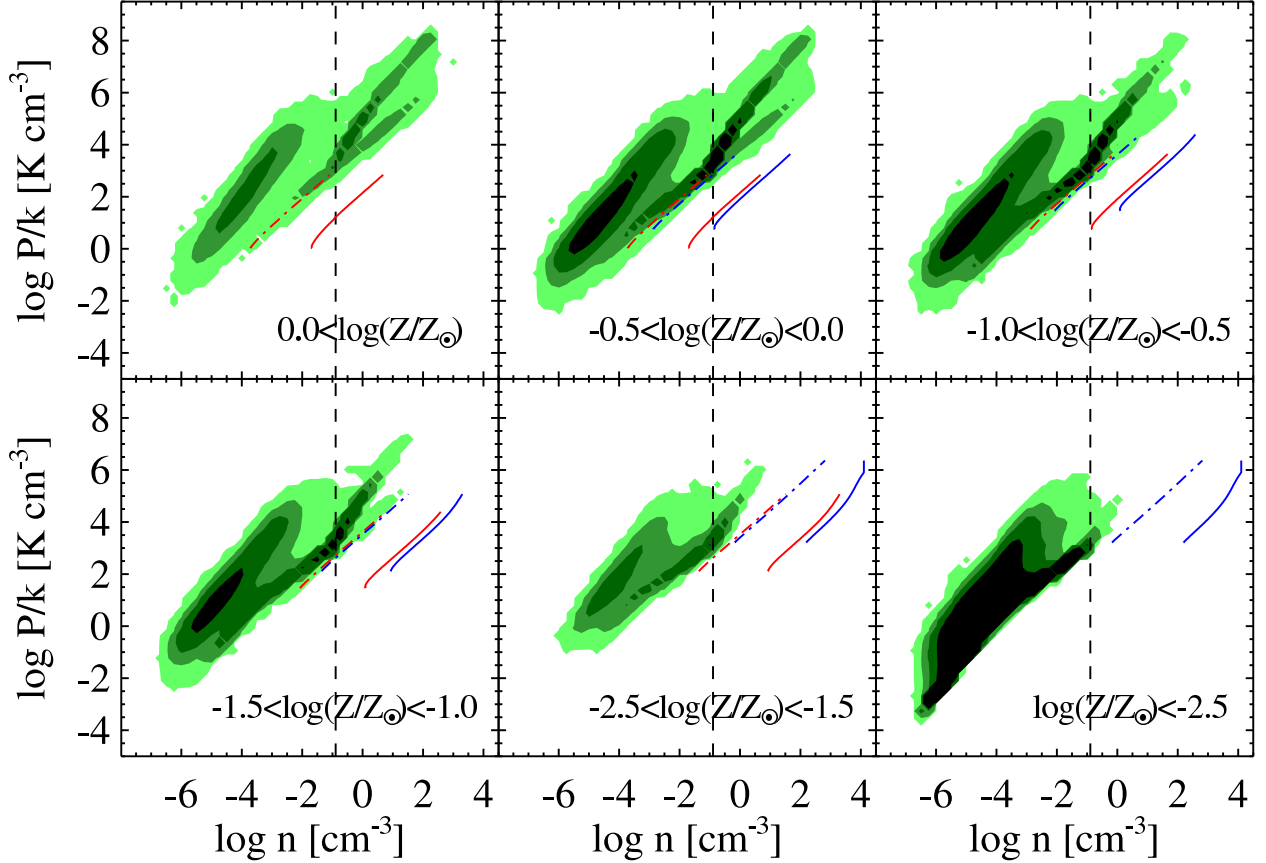


Fig. 5.— Density vs. pressure of the gas in the Q5 run at $z = 3$ for different metallicity ranges. The vertical dashed line is the same SF threshold density as shown in Figure 4. The two sets of lines indicate the P_{\min} for the lower (blue) and higher (red) metallicity limit of each panel as functions of WNM (*dot-dashed lines*) and CNM (*solid lines*) density, similarly to those lines shown in Figure 4. The lines for the WNM densities are shown because the criteria that we impose for the simulated gas to qualify for hosting CNM are $P > P_{\min}$ and $\rho_0 > \rho_W$ (see Equations [4] and [6]). The majority of the gas in the simulation that satisfy the pressure criteria $P > P_{\min}$ for the CNM is high metallicity gas. The contour levels are the same as in Figure 4.

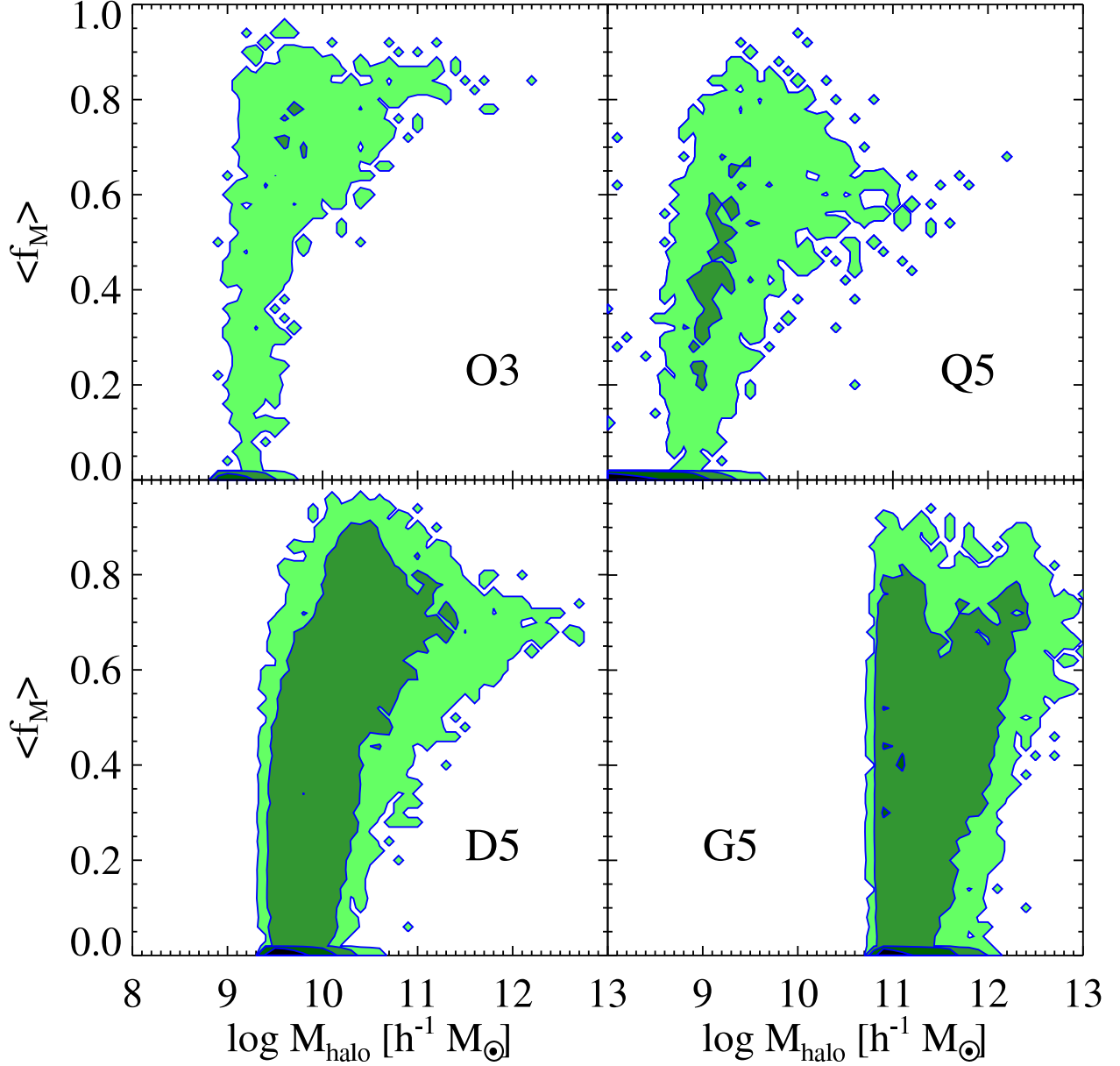


Fig. 6.— Mean mass fraction of CNM of each halo, $\langle f_M \rangle$, as a function of halo mass at $z = 3$. Each point on the figure represents the mean of f_M over all grid cells that cover each halo. The contours are used to avoid saturation in the scatter plot, and the four contour levels are for (1, 10, 100, 1000) data points in each two-dimensional bin of size $(\Delta \log M_{\text{halo}}, \Delta \langle f_M \rangle) = (0.1, 0.02)$ from low to high level. The two highest contour levels are not seen well as there is a large pool of data points with $\langle f_M \rangle = 0.0$, particularly for low mass halos in each run. The rapid decline of $\langle f_M \rangle$ values at $10 < \log M_{\text{halo}} < 12$ for the D5 and G5 run owes to lower resolution in simulations with large box-sizes, and we consider that the true decline occurs at around $M_{\text{halo}} \sim 10^{8.5} h^{-1} M_{\odot}$ (see text).

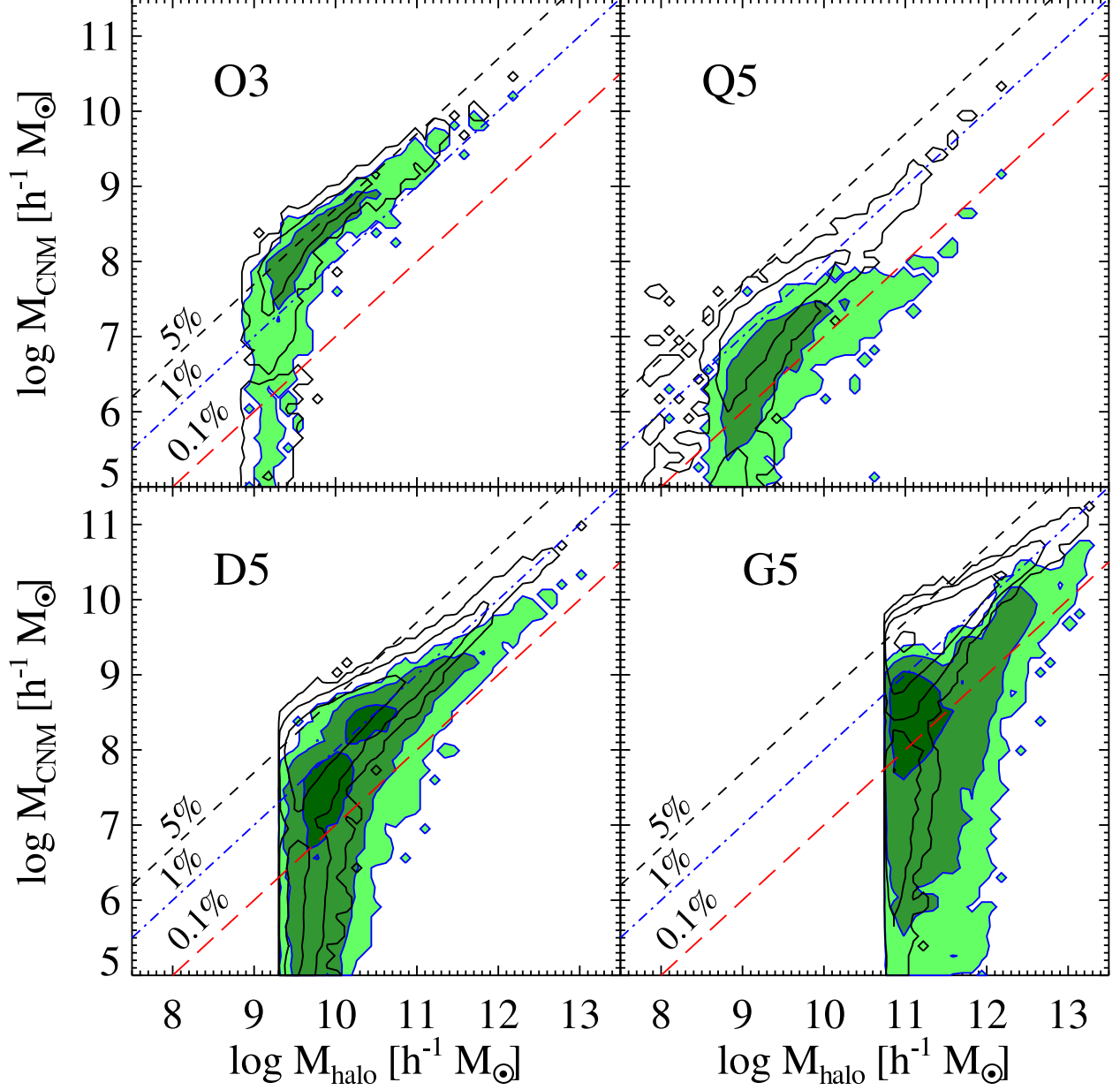


Fig. 7.— Shaded contours show the CNM mass of each halo as a function of dark matter halo mass at $z = 3$ in the simulations. The three contour levels are for (1, 10, 100) data points in each two dimensional bin of size $(\Delta \log M_{\text{halo}}, \Delta \log M_{\text{CNM}}) = (0.12, 0.13)$ from low to high level. The black contour lines without the shade is the total neutral gas mass within each dark matter halo, i.e., the maximum amount of CNM that each halo could host.

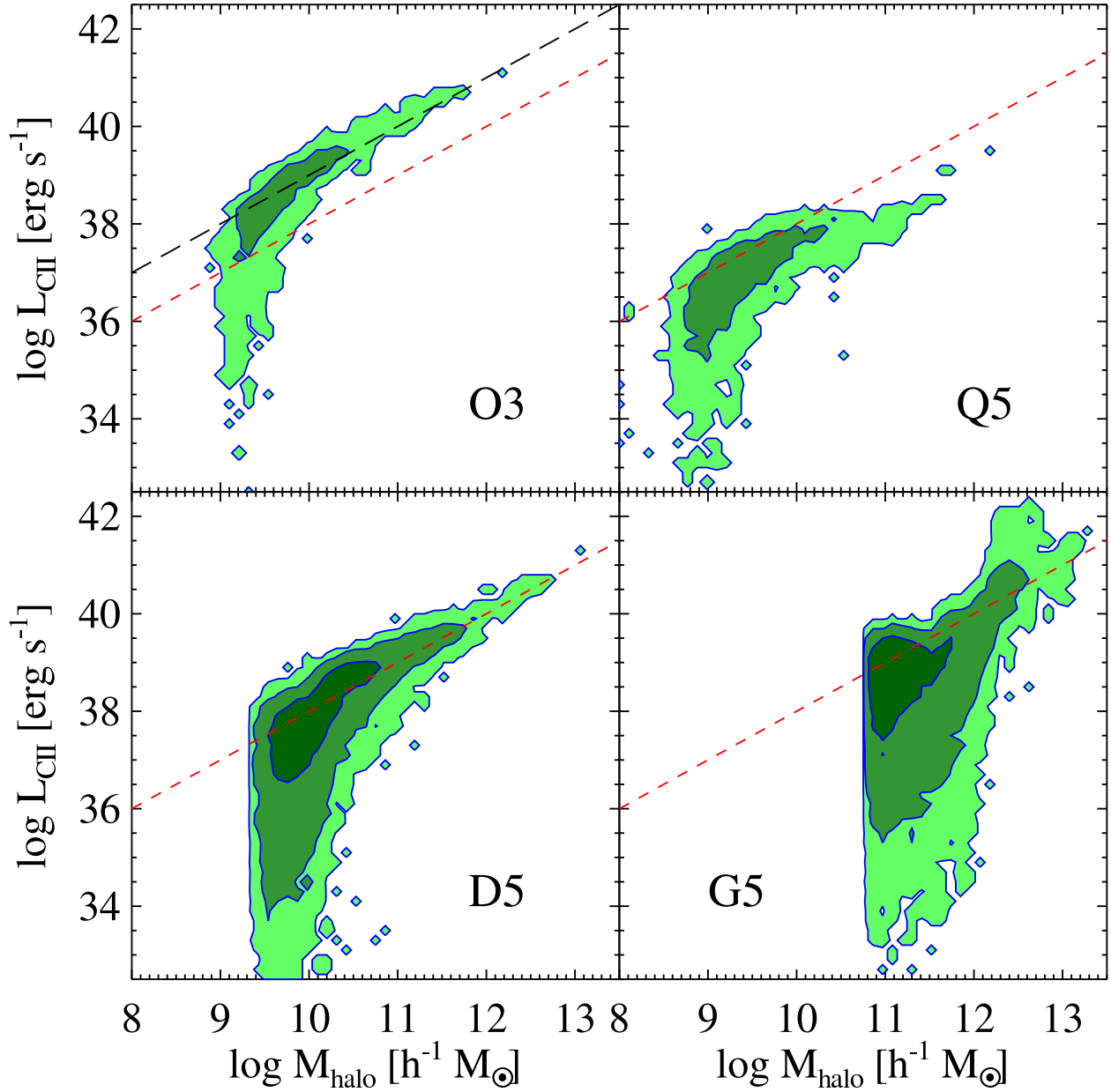


Fig. 8.— [C II] luminosity of each dark matter halo as a function of halo mass at $z = 3$. Each point in this plot represents a single halo, but we use contours to avoid saturation of points in the scatter plot. The 3 contour levels are for (1, 10, 100) data points in each 2-dimensional bin of size $(\Delta \log M_{\text{halo}}, \Delta \log M_{\text{CII}}) = (0.11, 0.20)$ from low to high level. The *long-dashed* line in the top left panel and the *short-dashed* line in other panels show the relationship $L_{\text{CII}} = C_1 (M_{\text{halo}}/10^{12} h^{-1} M_{\odot})$, where $C_1 = 10^{41}$ and $10^{40} \text{ erg s}^{-1}$, respectively.

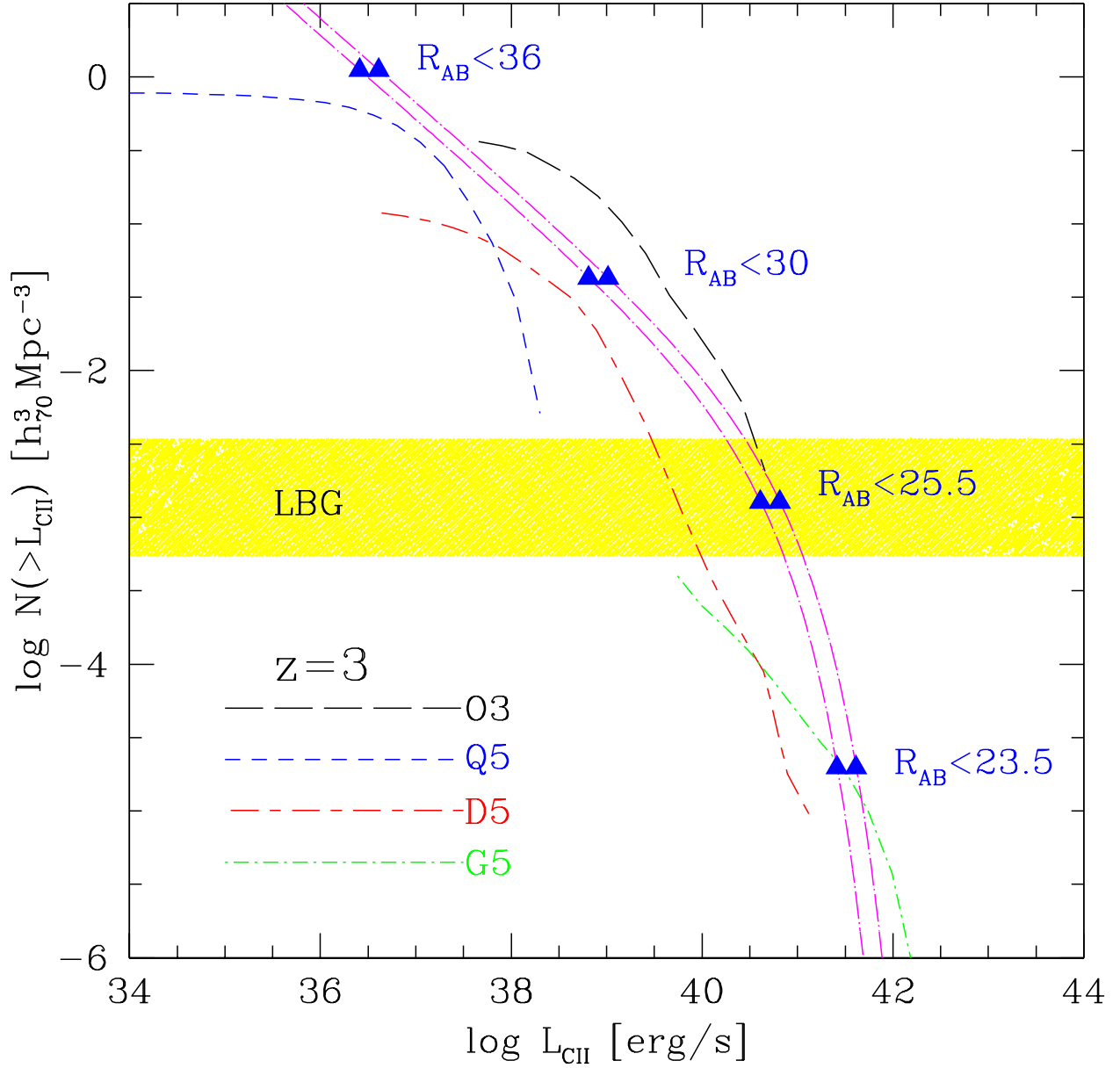


Fig. 9.— Cumulative [C II] luminosity function of simulations at $z = 3$. The ordinate is in units of comoving $h_{70}^3 \text{ Mpc}^{-3}$. The faint-end is truncated for the D5 and G5 run because of resolution limitations, and the bright-end of the O3 and Q5 runs is limited by cosmic variance owing to small simulation box-sizes. Note that the O3 run predicts a much higher [C II] luminosity than the Q5 run because of less efficient galactic wind feedback which allows more neutral gas to remain within the dark matter halos and emit [C II] line radiation. The yellow shaded region indicates the observed number density of LBGs brighter than $R_{\text{AB}} = 25.5$ at $z = 3$: $n_{\text{LBG}} = 4 \times 10^{-3} h^3 \text{ Mpc}^{-3}$ (Adelberger & Steidel 2000; Adelberger et al. 2003). See text for the details on the two magenta *dot-long-dashed* curves, which are derived from simple scaling laws between halo mass and R_{AB} magnitude of LBGs and their observed luminosity function.

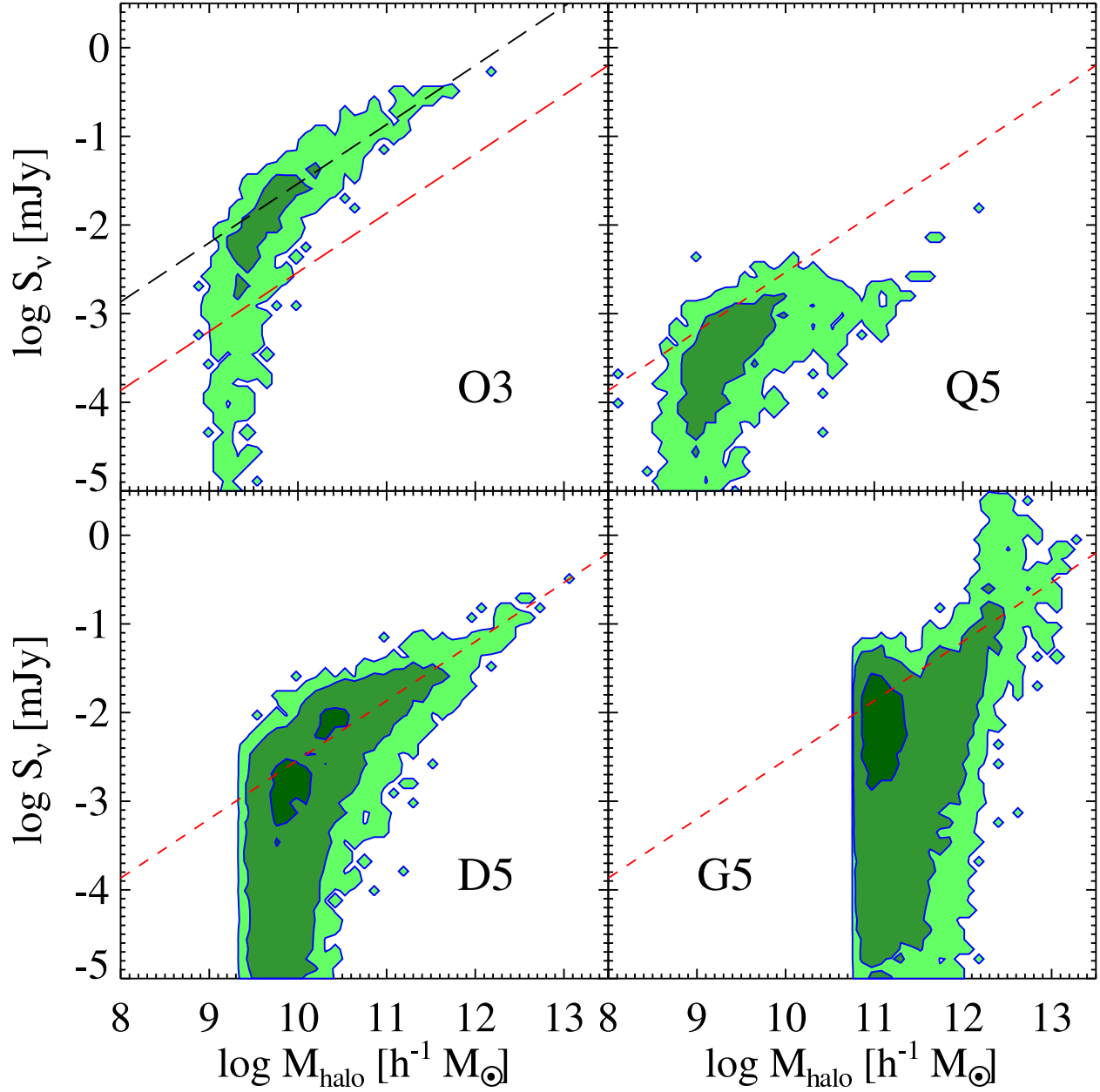


Fig. 10.— [CII] flux density of each dark matter halo as a function of halo mass at $z = 3$. The 3 contour levels are for (1, 10, 100) data points in each 2-dimensional bin of size $(\Delta \log M_{\text{halo}}, \Delta \log S_\nu) = (0.11, 0.13)$ from low to high. The *long-dashed* line in the top left panel and the *short-dashed* line in other panels show the relationship $\log S_\nu = \frac{2}{3}(\log M_{\text{halo}} - 12) + C_2$, where $C_2 = -0.2$ and -1.2 , respectively.

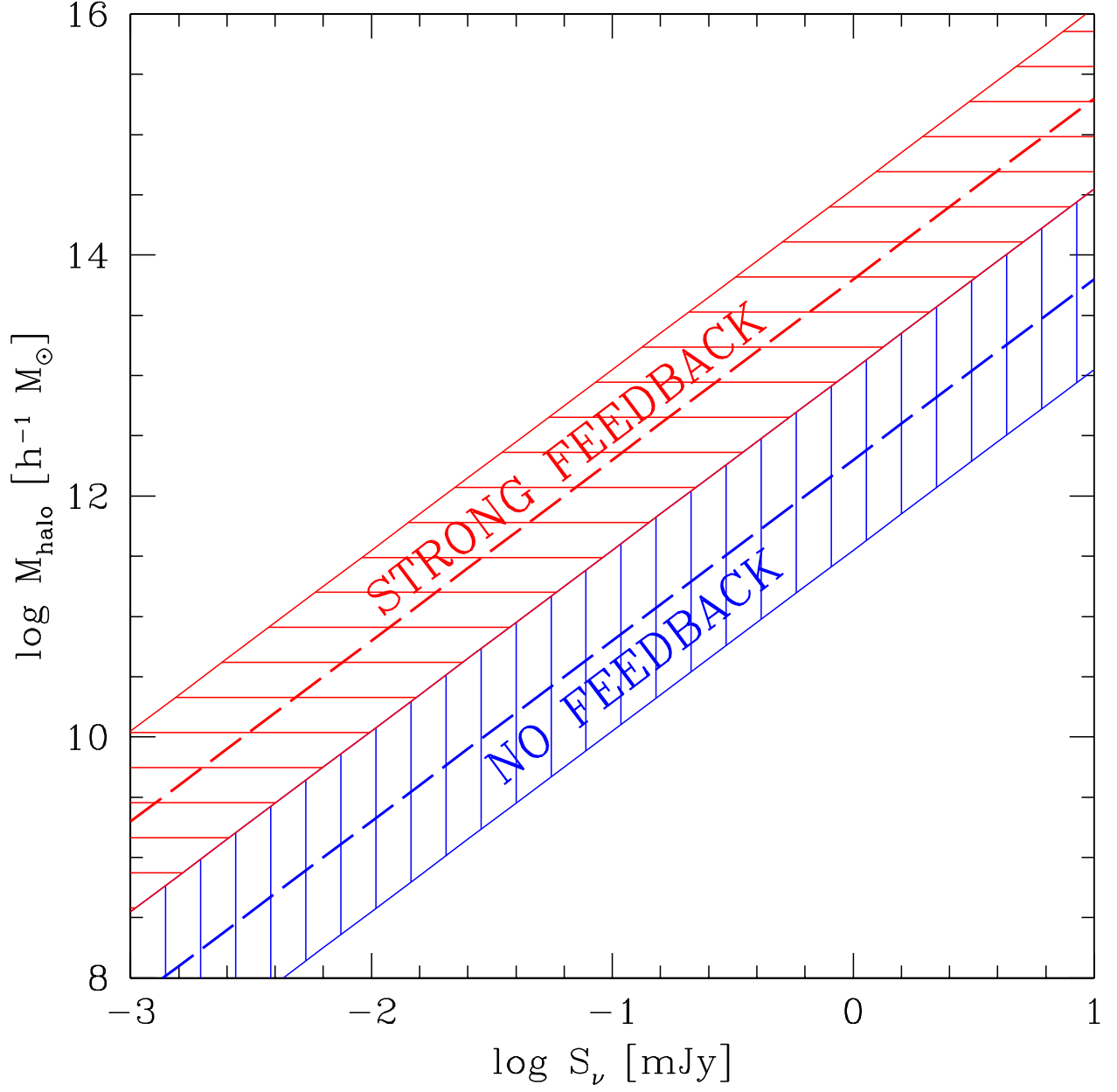


Fig. 11.— This figure shows the lowest limiting halo mass one can probe for a given flux density limit, summarizing Figure 10. The dashed lines are the same scalings shown in Figure 10, and the shaded region shows the dispersion of ± 0.5 dex at a given flux density around the scaling relation.

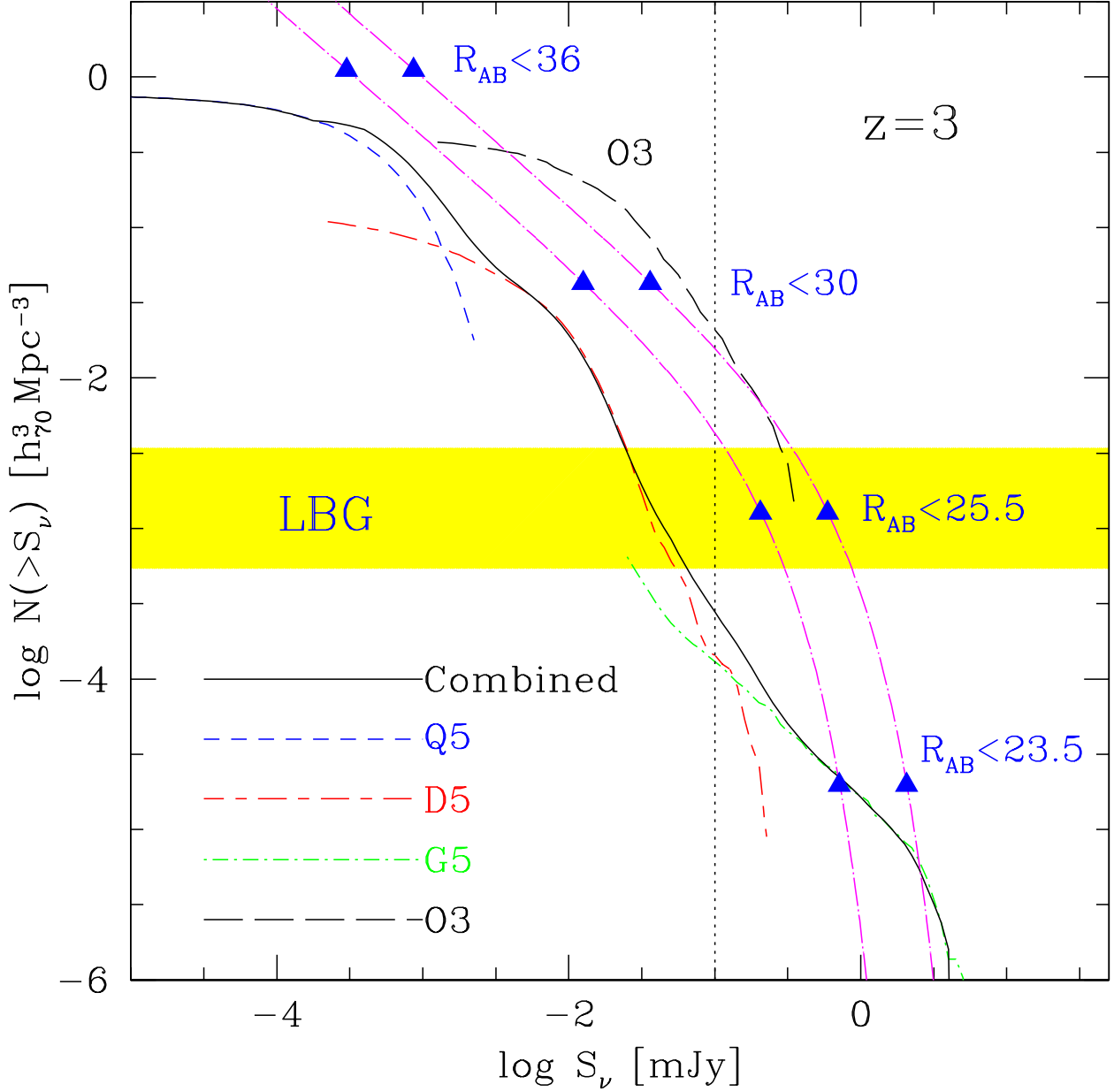


Fig. 12.— Cumulative [C II] flux density functions for O3, Q5, D5, G5 runs and the combined result of the latter 3 results. The ordinate is in units of comoving $h_{70}^3 \text{Mpc}^{-3}$. The rough detection limit of $S_\nu = 0.1 \text{mJy}$ for ALMA and SPICA is indicated by the vertical dotted line. The difference between the results of the O3 and Q5 runs owes to the difference in the strength of galactic wind feedback. The yellow shaded region indicates the observed number density of LBGs brighter than $R_{AB} = 25.5$ at $z = 3$: $n_{\text{LBG}} = 4 \times 10^{-3} h^3 \text{Mpc}^{-3}$ (Adelberger & Steidel 2000; Adelberger et al. 2003). See text for the details on the two magenta *dot-long-dashed* curves, which are derived from simple scaling laws between halo mass and R_{AB} magnitude of LBGs and their observed luminosity function.

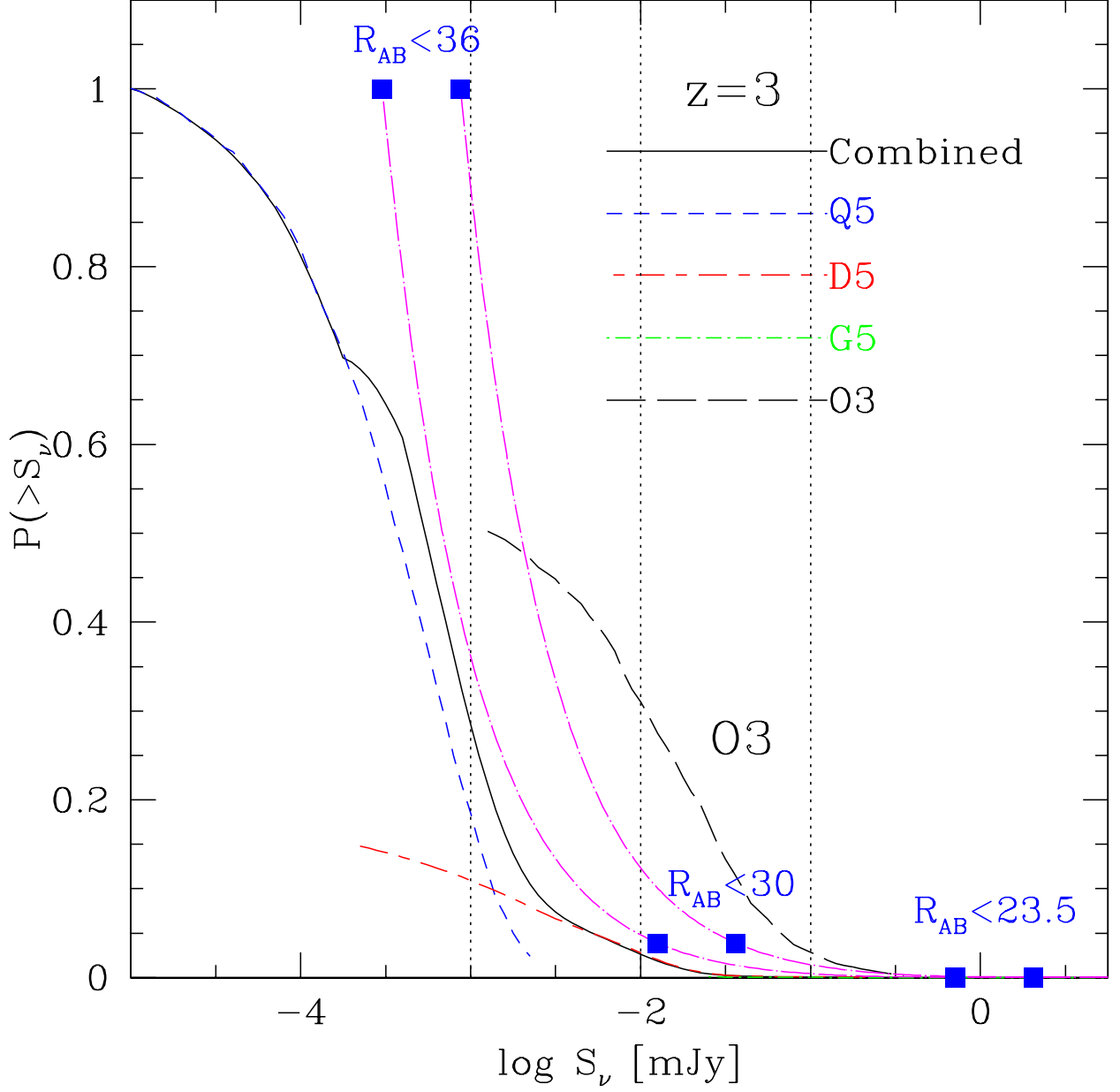


Fig. 13.— Cumulative probability distribution of [C II] sources as a function of flux density S_ν for the same models shown in Figure 12. It is seen that the majority of the sources are faint objects with $S_\nu < 0.1$ mJy. This suggests that one has to aim at very bright LBGs in order to have a detection even with ALMA and SPICA.